Adjustable corrosion and mechanical properties of Mg-Zn-Ca-Ni alloys for fracturing materials

Wang, Dawei; Jiang, Xiangshuang; Chen, Changxin; Zhang, Xun; Jin, Zhong Zheng; Cao, Fuyong; Zhu, Jia Ning; Wang, Cheng; Ma, Yinlong; Zha, Min

DOI
10.1016/j.jma.2024.07.011

Publication date
2025

Document Version
Final published version

Published in
Journal of Magnesium and Alloys

Citation (APA)
Wang, D., Jiang, X., Chen, C., Zhang, X., Jin, Z. Z., Cao, F., Zhu, J. N., Wang, C., Ma, Y., & Zha, M. (2025). Adjustable corrosion and mechanical properties of Mg-Zn-Ca-Ni alloys for fracturing materials. *Journal of Magnesium and Alloys*, *13*(6), 2618-2635. https://doi.org/10.1016/j.jma.2024.07.011

KeAi
CHINESE ROOTS
GLOBAL IMPACT

Available online at www.keaipublishing.com/en/journals/journal-of-magnesium-and-alloys/

ScienceDirect

Journal of Magnesium and Alloys 13 (2025) 2618–2635

www.elsevier.com/locate/jma

Full Length Article

Adjustable corrosion and mechanical properties of Mg-Zn-Ca-Ni alloys for fracturing materials ☆

Dawei Wang [a], Xiangshuang Jiang [a], Changxin Chen [a], Xun Zhang [a], Zhong-Zheng Jin [b,*], Fuyong Cao [c], Jia-Ning Zhu [d], Cheng Wang [a], Yinlong Ma [e], Min Zha [a,f,g,*]

[a] Key Laboratory of Automobile Materials of Ministry of Education & School of Materials Science and Engineering, Nanling Campus, Jilin University, No. 5988 Renmin Street, Changchun 130025, PR China
[b] Key Laboratory of UV-Emitting Materials and Technology, Ministry of Education, Northeast Normal University, Changchun, 130024, PR China
[c] Center for Marine Materials Corrosion and Protection, College of Materials, Xiamen University, Xiamen 361005, PR China
[d] Department of Materials Science and Engineering, Delft University of Technology, the Netherlands
[e] College of Construction Engineering, Jilin University, Changchun 130026, China
[f] State Key Laboratory of Superhard Materials, Jilin University, Changchun, 130012, PR China
[g] International Center of Future Science, Jilin University, Changchun 130012, PR China

Received 3 April 2024; received in revised form 16 June 2024; accepted 4 July 2024
Available online 1 August 2024

Abstract

Two sets of alloys, Mg-Zn-Ca-xNi ($0 \leq x \leq 5$), have been developed with tunable corrosion and mechanical properties, optimized for fracturing materials. High-zinc artificial aged (T6) Mg-12Zn-0.5Ca-xNi ($0 \leq x \leq 5$) series, featuring a straightforward preparation method and the potential for manufacturing large-scale components, exhibit notable corrosion rates up to 29 mg cm^{-2} h^{-1} at 25 °C and 643 mg cm^{-2} h^{-1} at 93 °C. The high corrosion rate is primary due to the Ni–containing second phases, which intensify the galvanic corrosion that overwhelms their corrosion barrier effect. Low-zinc rolled Mg-1.5Zn-0.2Ca-xNi ($0 \leq x \leq 5$) series, characterizing excellent deformability with an elongation to failure of ~26%, present accelerated corrosion rates up to 34 mg cm^{-2} h^{-1} at 25 °C and 942 mg cm^{-2} h^{-1} at 93 °C. The elimination of corrosion barrier effect via deformation contributes to the further increase of corrosion rate compared to the T6 series. Additionally, Mg-Zn-Ca-xNi ($0 \leq x \leq 5$) alloys exhibit tunable ultimate tensile strengths ranging from ~190 to ~237 MPa, depending on their specific composition. The adjustable corrosion rate and mechanical properties render the Mg-Zn-Ca-xNi ($0 \leq x \leq 5$) alloys suitable for fracturing materials.

Keywords: Mg-Zn-Ca alloy; Fracturing material; Galvanic corrosion; Corrosion barrier.

1. Introduction

Recently, the multi-stage fracturing technique has been considered necessary for economically efficient oil/gas production in low permeability shale resources [1-3]. The fracturing tools play a pivotal role in this technique. After the fracturing process, the conventional fracturing balls and bridge plugs are typically removed through milling or drilling processes, which are both expensive and time-consuming. To address this challenge, degradable fracturing materials have been developed that can be dissolved in fracturing fluid. These materials eliminate the need for a drill-out process, making them highly promising for oil/gas exploration [4].

The degradable fracturing materials must possess excellent mechanical properties and a high degradable rate. In other words, they should be strong enough to withstand the high pressure during the fracturing process while also dissolving rapidly in the fracturing fluid afterwards [4-7]. Moreover,

☆ Peer review under responsibility of Chongqing University.

* Corresponding authors.
E-mail addresses: jinzz031@nenu.edu.cn (Z.-Z. Jin), minzha@jlu.edu.cn (M. Zha).

https://doi.org/10.1016/j.jma.2024.07.011

the mechanical properties and degradation rate should be adjustable to meet the diverse requirements of various components in bridge plugs [8].

Mg and its alloys feature a low density and high strength-to-weight ratio, making them widely used in the field of transportation, aerospace and so on [9,10]. Moreover, Mg alloys, with a standard electrochemical potential of −2.37 V, possess inherent electrochemically active and are promising candidates as degradable fracturing materials [11,12]. Additionally, their mechanical properties and corrosion rate can be tailored through microstructure optimization, making them suitable for various components in bridge plug. The mechanical strength of Mg alloys is typically improved through various strengthening mechanisms, such as precipitation strengthening, grain boundaries strengthening, solution strengthening and so on [13,14]. The corrosion rate of Mg alloys is primarily dominated by galvanic-corrosion [15-17].

In contrast to corrosion-resistant Mg alloys that strictly limit impurity elements, degradable Mg alloys can achieve high degradation rates by incorporating impurity elements such as Fe, Co, Cu, and Ni. Oh et al. [18] and Niu et al. [19] have demonstrated that the addition of Ni significantly increases the corrosion rate of Mg and Mg-4Zn based alloys due to the formation of noble Mg_2Ni phase. The Cu-containing phase acts as an active cathode, generating more galvanic couplings and thereby accelerating galvanic corrosion in Mg-17Al-3Zn and Mg-3Zn-1Y based alloys [20,21]. Fe, when presents as elemental substrate in Fe/Mg–Al–Zn matrix composite, produces more galvanic couplings and accelerate the corrosion rate [22,23].

The morphology and distribution of second phases also play a crucial role in determining the corrosion rate. In Mg-Ni-Y alloys, the long period stacking order (LPSO) phase has a complex effect on the corrosion rate. On the one hand, it can serve as a cathodic site, accelerating the corrosion process [24]. Consequently, the breakdown of the LPSO phase can significantly increase the corrosion rate of alloys due to the elimination of its corrosion barrier effect [25]. Wang et al. compared the corrosion rates of Mg-Al-Sn-Ca alloys produced by conventional solidification and sub-rapid solidification. It is observed that the alloy produced by sub-rapid solidification exhibits smaller and more evenly distributed CaMgSn phase, leading to the formation of more galvanic cells and consequently increasing the corrosion rate [26].

To achieve Mg alloys with adjustable mechanical and corrosion properties suitable for degradable fracturing materials, we designed two sets of alloys: the high-zinc T6 Mg-12Zn-0.5Ca-xNi ($0 \leq x \leq 5$) and the low-zinc rolled Mg-1.5Zn-0.2Ca-xNi ($0 \leq x \leq 5$) series. Mg-Zn alloys were selected here due to their excellent formability, while Ca was employed to refine grains and enhance mechanical properties. The addition of Ni was used to optimize the corrosion rate through control of galvanic corrosion. The high-zinc T6-Mg-12Zn-0.5Ca-xNi series are expected to gain strength from second phase and offer a simple, short manufacturing process. In contrast, the low-zinc Mg-1.5Zn-0.2Ca-xNi series aim to achieve strength through grain refinement and exhibit excellent deformability.

2. Experimental

2.1. Materials preparation

The investigated Mg-Zn-Ca-xNi alloys were casted using pure Mg (99 wt.%), pure Al (99 wt.%), pure Zn (99 wt.%), Mg-20Ca (wt.%) and Mg-25Ni (wt.%) master alloys, under the protection of mixed gas consisting of CO_2 and SF_6 (9:1) in a crucible resistance oven. The molten alloys were poured into an iron mold. The actual chemical composition of investigated samples was characterized using energy dispersive spectroscopy (EDS), and the resulting data is presented in Table 1. A multistep homogenization treatment (T4, 280 °C for 2 h, 325 °C for 6 h and 345 °C for 4 h) was carried out in a tube furnace with an argon atmosphere followed by water quenching for both high-zinc and low-zinc alloys. For the high-zinc Mg-12Zn-0.5Ca-xNi ($0 \leq x \leq 5$) series, an artificial aging (T6) treatment at 180 °C for 2 h was undertaken subsequently. For the low-zinc Mg-1.5Zn-0.2Ca-xNi ($0 \leq x \leq 5$) alloys, the specimen suffered 8-passes single direction hot-rolling at 100 °C afterwards, with a total reduction of 80%. The obtained sheets had a thickness of ∼1 mm, and were then annealed at 300 °C for 30 min.

2.2. Structure characterization

The microstructure was characterized using field emission scanning electron microscope (FESEM, ZEISS Sigma 500, Germany) equipped with energy dispersive spectrometer (EDS) analyzer (OXFORD X-Max^N AZtec) and electron back-scatter diffraction (EBSD) detector (OXFORD NordlysNano AZtec). The alloys were grounded and chemically etched using a liquid mixture of 5 g picric acid + 5 ml acetic acid + 10 ml distilled water + 80 ml ethanol for ∼ 5-9 s. EBSD samples were electro-polished at 20 V for ∼90 s. The phase analysis was conducted by X-ray diffraction (XRD, Model D Max 2500PC Rigaku Japan) with Cu-K radiation under 50 kV and 250 mA at a scan rate of 2° min^{-1}. Differential scanning calorimetry (DSC) was carried out to confirm the phase composition. The 3D corrosion morphology was characterized by laser scanning confocal microscopy (LSCM, OLS3000). Scanning Kelvin probe force microscopy (SKPFM) tests of the alloys were performed using an atomic force microscope (Dimension Icon, Bruker). Surface potential measurements were performed in non-contact mode using a magnetically etched silicon probe (MESP-V2, K = 3 N/m, f_0 = 75 kHz, Bruker Corporation, CA, USA) at 25 °C and a maintained relative humidity of 40%. The data of surface potential distribution were analyzed with NanoScope Analysis 3.0 software.

2.3. Mechanical test

The mechanical properties of the investigated alloys were studied by a tensile testing machine (AGS-X, Shimadzu,

Table 1
The actual chemical composition of Mg-Zn-Ca-xNi alloys.

Alloy	Mg (wt.%)	Zn (wt.%)	Ca (wt.%)	Ni (wt.%)
T6 Mg-12Zn-0.5Ca-0Ni	Bal.	10.4	0.6	—
T6 Mg-12Zn-0.5Ca-0.5Ni	Bal.	12.3	0.8	0.5
T6 Mg-12Zn-0.5Ca-1Ni	Bal.	12.4	0.8	0.7
T6 Mg-12Zn-0.5Ca-2Ni	Bal.	11.2	0.7	1.8
T6 Mg-12Zn-0.5Ca-3Ni	Bal.	10.3	0.6	2.5
T6 Mg-12Zn-0.5Ca-5Ni	Bal.	9.9	0.4	4.8
Rolled Mg-1.5Zn-0.2Ca-0Ni	Bal.	1.6	0.3	—
Rolled Mg-1.5Zn-0.2Ca-1Ni	Bal.	1.5	0.4	1.1
Rolled Mg-1.5Zn-0.2Ca-3Ni	Bal.	1.7	0.2	3.1
Rolled Mg-1.5Zn-0.2Ca-5Ni	Bal.	1.6	0.2	5.2

Japan) using the Shimadzu AGS-X detection system. The dog-bone-shaped specimens, having a gage length of 30 mm and width of 10 mm, were polished with 1000 # sandpaper prior to testing. Tensile tests were conducted both at room temperature and 93 °C, with a strain rate of 1.0×10^{-3} s^{-1}. At least three parallel samples were tested, and the centralized value of the sample was taken as the performance indicator.

2.4. Corrosion test

The corrosion properties were tested by immersing specimens in a 3.5 wt.% NaCl solution at 25 °C and 93 °C, respectively. The specimens were mounted by epoxy resin with an exposed area of 10 × 10 mm^2. To maintain the experimental conditions at 93 °C, a water bath heating device was utilized, and the beaker was sealed with a sealing film to recycle the volatilization of the solution, thereby preventing any variation in NaCl concentration during the test. Hydrogen volume was recorded during immersion. Five specimens were measured for individual test to guarantee the reproducibility of the data. The corrosion rate was calculated by equation [27,28]:

$$P_H = 2.088V_H \tag{1}$$

Where P_H is the hydrogen evolution corrosion rate in mm y^{-1}, V_H is the hydrogen evolution rate in mL cm^{-2} d^{-1}.

After immersion test, the specimens were cleaned with chromate solution (200 g L^{-1} CrO_3 + 10 g L^{-1} $AgNO_3$) for 10 min to remove the corrosion products, followed by washing with the alcohol. Then, the specimens were dried by hot air flow. The weights of specimens before and after immersion were recorded to obtain the weight loss. The weight loss corrosion rate was calculated by equation [29]:

$$P_w = \frac{2.10(W_a - W_b)}{At} \tag{2}$$

Where P_w is the weight loss corrosion rate in mm y^{-1}, W_a is the weight of specimens before immersion in mg, W_b is the weight of specimens after immersion without corrosion products in mg. A is the surface area of specimens in cm^2, and t is the total immersion time in day.

Electrochemical tests were performed in a three-electrode cell using a PAR VersaSTAT 3F electrochemical workstation. The investigated alloys act as working electrode, platinum foil as counter electrode and saturated calomel as reference electrode. Open circuit potential (OCP), electrochemical impedance spectroscopy (EIS), and potentiodynamic polarization (PDP) were carried out successively. Open circuit test was carried out for 900 s to monitor the solid/liquid interface. EIS measurement was performed in the frequency range of 100 kHz – 1 Hz with an amplitude of 5 mV. EIS plots were fitted using ZView software. Potentiodynamic polarization was undertaken between −1.2 V and +1.2 V (vs OCP) at a scan rate of 0.5 mV s^{-1}. Tafel extrapolation method was used to fit the polarization curves via VersaStudio software. The corrosion current density i_{corr} (mA cm^{-2}) was used to evaluate the corrosion rate P_i (mm y^{-1}) by equation [30]:

$$P_i = 22.85 i_{corr} \tag{3}$$

The equivalent capacitance C_{dl} related to CPE_{dl} was calculated by equation [31]:

$$C_{dl} = CPE_{dl}^{\frac{1}{n}} \left(\frac{1}{R_S} + \frac{1}{R_{ct}} \right)^{\frac{n-1}{n}} \tag{4}$$

Where C_{dl} is the value of CPE-T, R_S is solution resistance, R_{ct} is the charge transfer resistance between Helmholtz double layer, and n represents a parameter between 0 and 1. All the parameters were achieved from the fitting results of EIS plots.

3. Results

3.1. Microstructure of Mg-Zn-Ca-xNi (0 ≤ x ≤ 5) alloys

Fig. 1 shows the SEM images of as-cast Mg-12Zn-0.5Ca-xNi ($0 \le x \le 5$) alloys. Numerous eutectic phases are imbedded in α-Mg matrix, with an increasing area fraction of 8.4%, 8.5%, 7.9%, 9.2%, 12.7% and 19.0% for x = 0, 0.5, 1, 2, 3, 5, respectively. Meanwhile, the distribution of eutectic phases changes from semi-closed network to closed network.

Energy dispersive spectroscopy (EDS) was carried out to detect the element distribution and differentiate the eutectic phase in Mg-12Zn-0.5Ca-xNi ($0 \le x \le 5$) alloys (Fig. 2). Zn nearly covers all the eutectic phase, and Ca is rich in partial eutectic phase. For x = 0, the eutectic phases are MgZn and CaMgZn, respectively (Fig. 2a). For Ni-containing alloys, the introduced Ni and original Ca are mutually exclusive and distribute separately in different eutectic phases. The

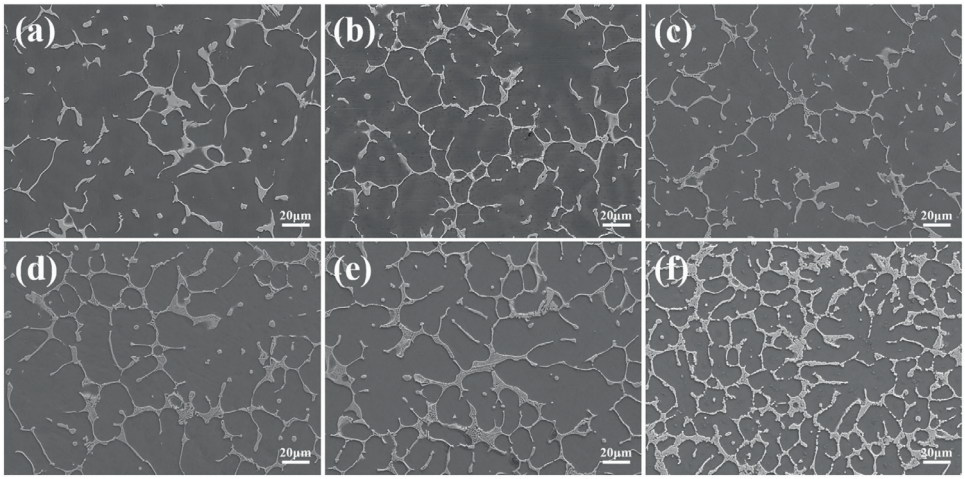

Fig. 1. SEM images of as-cast Mg-12Zn-0.5Ca-xNi ($0 \leq x \leq 5$) alloys: (a) $x = 0$, (b) $x = 0.5$, (c) $x = 1$, (d) $x = 2$, (e) $x = 3$, (d) $x = 5$.

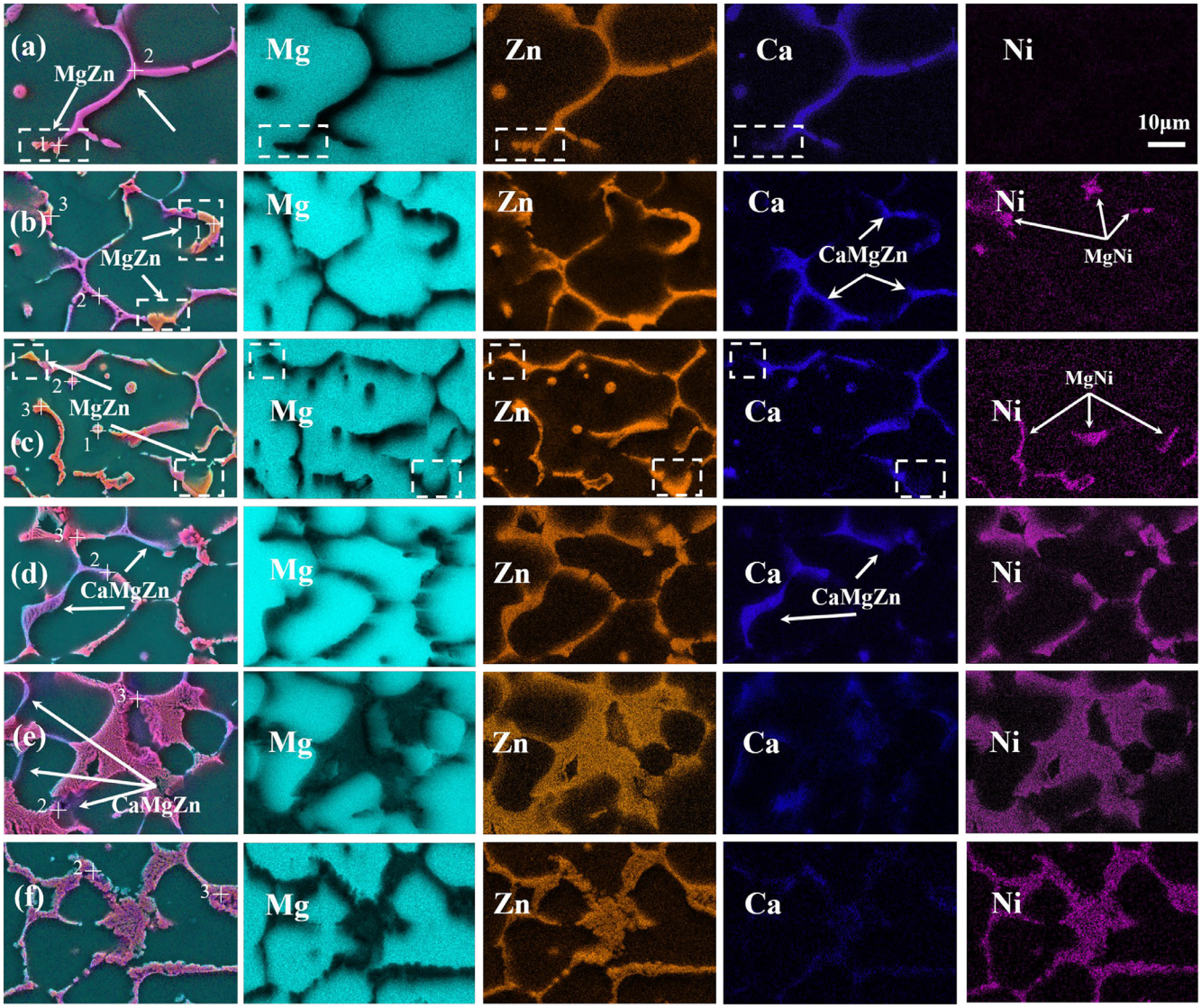

Fig. 2. Energy dispersive spectroscopy (EDS) images of as-cast Mg-12Zn-0.5Ca-xNi ($0 \leq x \leq 5$) alloys: (a) $x = 0$, (b) $x = 0.5$, (c) $x = 1$, (d) $x = 2$, (e) $x = 3$, (f) $x = 5$.

Table 2
Composition and fraction of eutectic phase in as-cast Mg-12Zn-0.5Ca-xNi ($0 \leq x \leq 5$) alloys.

	Mg: Zn: Ca: Ni			Eutectic phase	Fraction (%)
	1	2	3		
$x = 0$	8:2:0:0	6:3:1:0	——	Mg_7Zn_3, Mg_2Zn_3, $Ca_2Mg_6Zn_3$	8.4
$x = 0.5$	6:3:0:0	6:3:1:0	5:4:0:1	Mg_7Zn_3, Mg_2Zn_3, MgZnNi, $MgZn_2$, $Ca_2Mg_6Zn_3$	8.5
$x = 1$	7:2:0:0	5:4:1:0	4:5:0:1	Mg_7Zn_3, Mg_2Zn_3, MgZnNi, $MgZn_2$, $Ca_2Mg_6Zn_3$	7.9
$x = 2$	——	7:2:1:0	7:2:0:1	MgZnNi, $MgZn_2$, $Ca_2Mg_6Zn_3$	9.2
$x = 3$	——	7:1:1:0	7:2:0:1	MgZnNi, $MgZn_2$, $Ca_2Mg_6Zn_3$	12.7
$x = 5$	——	9:1:0:0	6:2:0:1	MgZnNi, $MgZn_2$, $Ca_2Mg_6Zn_3$	19.0

phenomenon supports that the introduced Ni elements cluster with Mg and Zn elements rather than Ca element, forming a ternary MgZnNi eutectic phases [32]. With the increase of Ni content, more MgZnNi phases form and the MgZn particles disappear when the Ni content is larger than 2. Meanwhile, the area fraction of CaMgZn phase seems decrease, which might be covered by the incremental MgZnNi phases. Furthermore, the stoichiometry of the eutectic phases was counted by EDS, and is summarized in Table 2.

X-ray diffraction (XRD) and differential scanning calorimetry (DSC) measurements were conducted to confirm the eutectic phases and determine the homogenization temperature. The main peaks of XRD patterns are derived from α-Mg matrix, while the minor peaks are attributed to Mg_7Zn_3, Mg_2Zn_3, $MgZn_2$, τ (MgZnNi), Mg_2Ni and $Ca_2Mg_6Zn_3$ phases [18,19,32] (Fig. 3a and Table 2). Noted that Mg_7Zn_3 and Mg_2Zn_3 phases exist when the Ni content is low ($0 \leq x \leq 2$). τ (MgZnNi) is formed once the Ni is introduced, and Mg_2Ni could be observed at high Ni content ($x = 3$ and 5). $MgZn_2$ and $Ca_2Mg_6Zn_3$ phases exist in all alloys. Three endothermal peaks at 336, 353 and 600 °C are observed in DSC curves for $x = 0$, corresponding to the melt of Mg_7Zn_3, Mg_2Zn_3, and α-Mg matrix, respectively [19,33]. With the increase of Ni content, the endothermal peaks attributing to Mg_7Zn_3 and Mg_2Zn_3 peaks decrease in intensity and disappear at $x = 2$. Instead, a shoulder peak appears and keeps shifting to high temperature side, indicating the continuous incorporation of Ni element in τ (MgZnNi) phase. The endothermal peak at 462 °C is related to the dissolution of stable phases, such as $MgZn_2$ and $Ca_2Mg_6Zn_3$ [34,35]. However, the reason for its absence at $x = 0$, 0.5, 1 is unclear yet (Fig. 3b). The phases identified by XRD and DSC are consistent with the composition detected by EDS results.

According to SEM, EDS images, XRD patterns, and DSC curves (Fig. 3b), alloys exhibit diverse second phases with varying melting points. Therefore, a multi-step homogenization approach was formulated to gradually melt the second particles from lower to higher melting points, aiming to prevent overburning of the lower-melting phases and uneven melting of the higher-melting phases.

After artificial aging treatment (T6), the microstructure exhibits negligible change compared to that of as-cast alloys, except for the slight dissolution of eutectic particle from the edges (Fig. S1). The indistinctive structure change might be attributed to the high alloying content, and low solubility limit

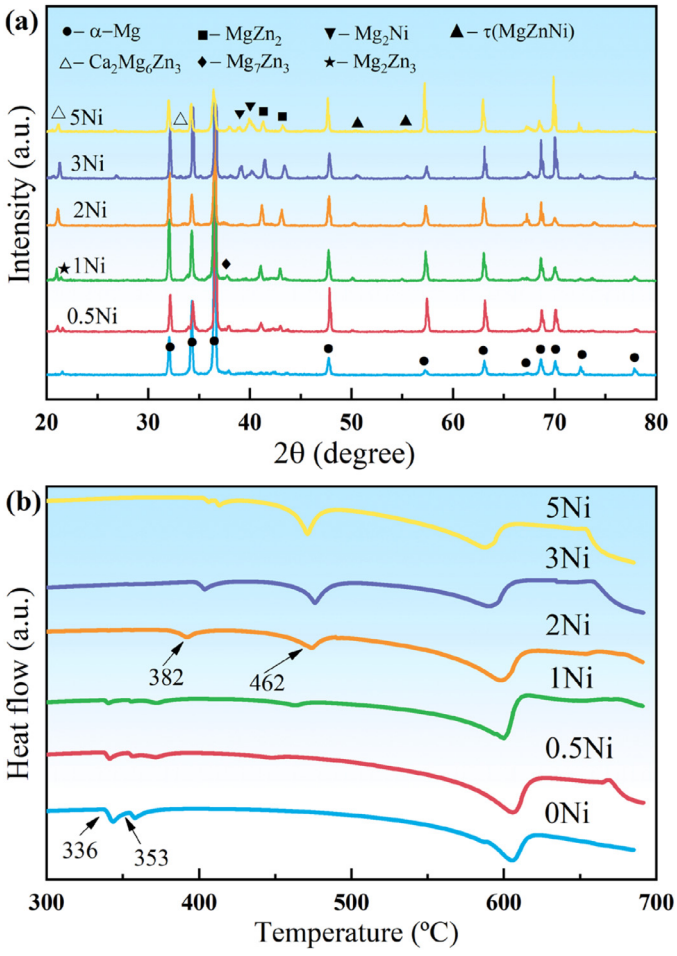

Fig. 3. Phase identification and relative thermal behaviors of as-cast Mg-12Zn-0.5Ca-xNi ($0 \leq x \leq 5$) alloys: (a) XRD patterns, (b) DSC curves.

of Zn and Ni in α-Mg matrix. The abundant refractory phases would affect the mechanical properties and degradation tendency of T6 Mg-12Zn-0.5Ca-xNi ($0 \leq x \leq 5$) alloys greatly.

As to the as-cast Mg-1.5Zn-0.2Ca-xNi ($0 \leq x \leq 5$) alloys, the eutectic phases exhibit a semi-closed or closed network structure likewise. However, the network structure is much sparser compared to that of Mg-12Zn-0.5Ca-xNi ($0 \leq x \leq 5$) alloys, due to the low Zn content. Apparently, the closed network becomes denser with Ni introduction (Fig. 4a-d). In addition, the homogenization treatment scarcely modifies the morphology of eutectic phases, excepted for the faintly

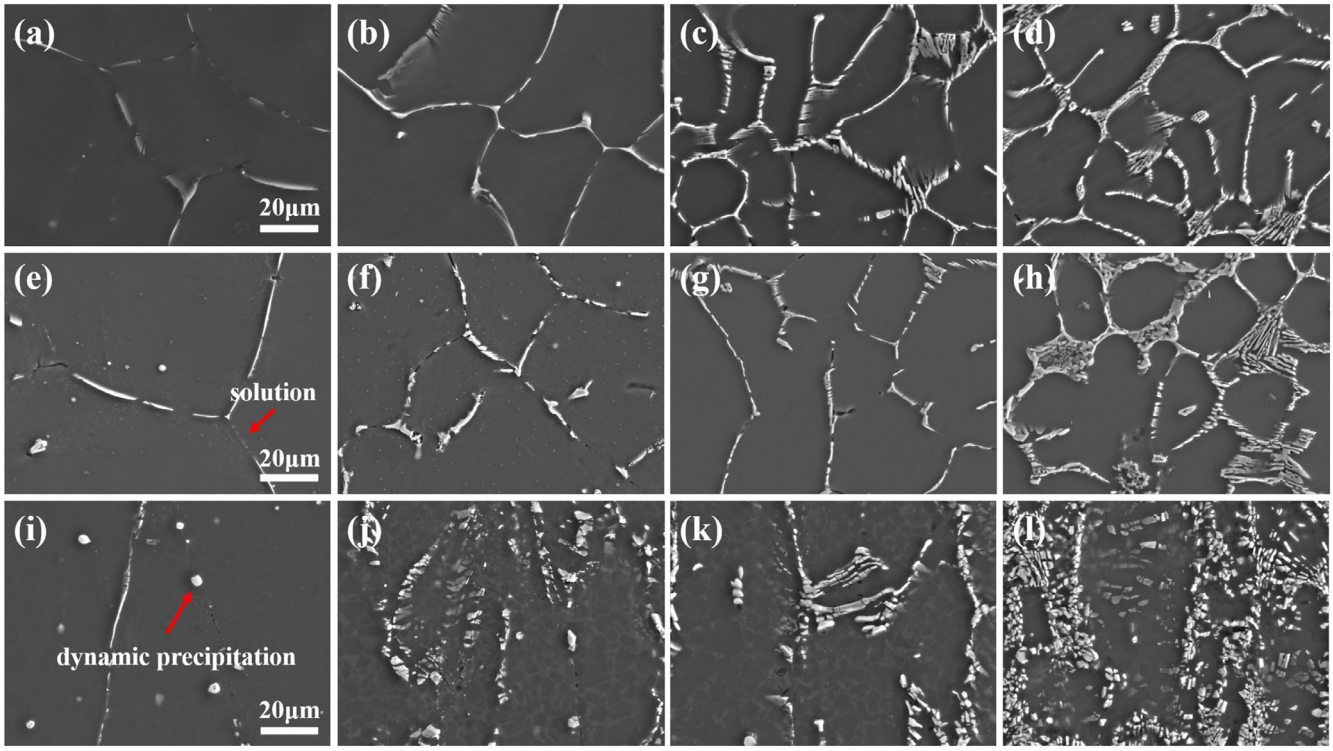

Fig. 4. SEM images of (a-d) as-cast, (e-h) T4 and (i-l) rolled Mg-1.5Zn-0.2Ca-xNi ($0 \leq x \leq 5$) alloys: (a, e, i) $x = 0$, (b, f, j) $x = 1$, (c, g, k) $x = 3$, (d, h, l) $x = 5$.

dissolution of network (Fig. 4e-h). After rolling, the enclosed networks are smashed into isolated small particles, which distribute randomly in α-Mg matrix (Fig. 4i-l).

EDS mappings show that for $x = 0$ specimen, Zn and Ca are nearly overlapped, indicating the domination of CaMgZn phase and lack of MgZn phases. With the increase of Ni content, the signal of Zn and Ca weakens in eutectic particles. Similar with Mg-12Zn-0.5Ca-xNi alloys, Ca and Ni are mutually exclusive and distribute separately (Fig. 5). Because the limited Zn is bound in $Ca_2Mg_6Zn_3$ phase, the introduced Ni reacts with Mg matrix after the quick consumption of Zn element, forming Mg_2Ni after τ (MgZnNi) phase [36,37]. With the increase of Ni content, the signal of Mg_2Ni intensifies (Fig. 6). Meanwhile, the signal of $Ca_2Mg_6Zn_3$ decreases, which might be due to the possible coverage by Mg_2Ni Phase.

Fig. 7 presents EBSD of the rolled alloys. Obviously, the grain size undergoes a significant reduction after rolling. In addition, the grain size decreases slightly with Ni alloying, i.e., about 5.2, 4.1, 3.9 and 5.3 μm for $x = 0$, 1, 3, 5, respectively. The texture intensity ranges from 3.51 to 4.54 for the alloys, reflecting a negligible textural evolution with Ni alloying.

3.2. Corrosion behavior of Mg-Zn-Ca-xNi ($0 \leq$ x ≤ 5) alloys

The corrosion property plays a vital role in the fracturing materials, and was evaluated through H_2 evolution experiment (Fig. 8a, b). The H_2 volume was collected within 12 h and 200 min at 25 °C for T6 Mg-12Zn-0.5Ca-xNi ($0 \leq x \leq 5$) and rolled Mg-1.5Zn-0.2Ca-xNi ($0 \leq x \leq 5$) alloys, due to the concern of corrosion penetration and their different thickness, i.e., ~5 mm and ~1 mm. For Mg-Zn-Ca-xNi ($0 \leq x \leq 5$) alloys, the H_2 volume increases linearly with immersion, indicating a constant degradation rate. The linear H_2 volume vs immersion time makes the comparison of corrosion rate meaningful, although the test time is not same. Noted that the alloys exhibit a faster H_2 evolution with incremental Ni content, indexing a higher corrosion rate. The corrosion rate calculated by H_2 evolution is shown in Table 3. After the H_2 evolution test, the weight loss was calculated, and the corresponding corrosion rate are displayed in Fig. 8c and summarized in Table 3. Both P_H and P_W show the similar trend with Ni content. For alloy $x = 0$, the corrosion rates of T6 Mg-12Zn-0.5Ca and rolled Mg-1.5Zn-0.2Ca alloys are similar, indicative of the massive MgZn/CaMgZn phases (8.4%) do not affect the corrosion rate significantly. In contrast, the corrosion rate increases severely with the addition of Ni for both T6 Mg-12Zn-0.5Ca-5Ni and rolled Mg-1.5Zn-0.2Ca-5Ni alloys. Moreover, rolled Mg-1.5Zn-0.2Ca-xNi ($0 \leq x \leq 5$) alloys always exhibit a higher corrosion rate than T6-Mg-12Zn-0.5Ca-xNi ($0 \leq x \leq 5$) alloys at the same Ni content.

To accurately replicate the realistic operational conditions for fracturing materials during gas/oil exploration, the temperature of the corrosion medium was precisely set at 93 °C (Fig. 8). H_2 volume increases linearly for Mg-Zn-Ca-xNi ($0 \leq x \leq 5$) alloys during short immersion time, and then

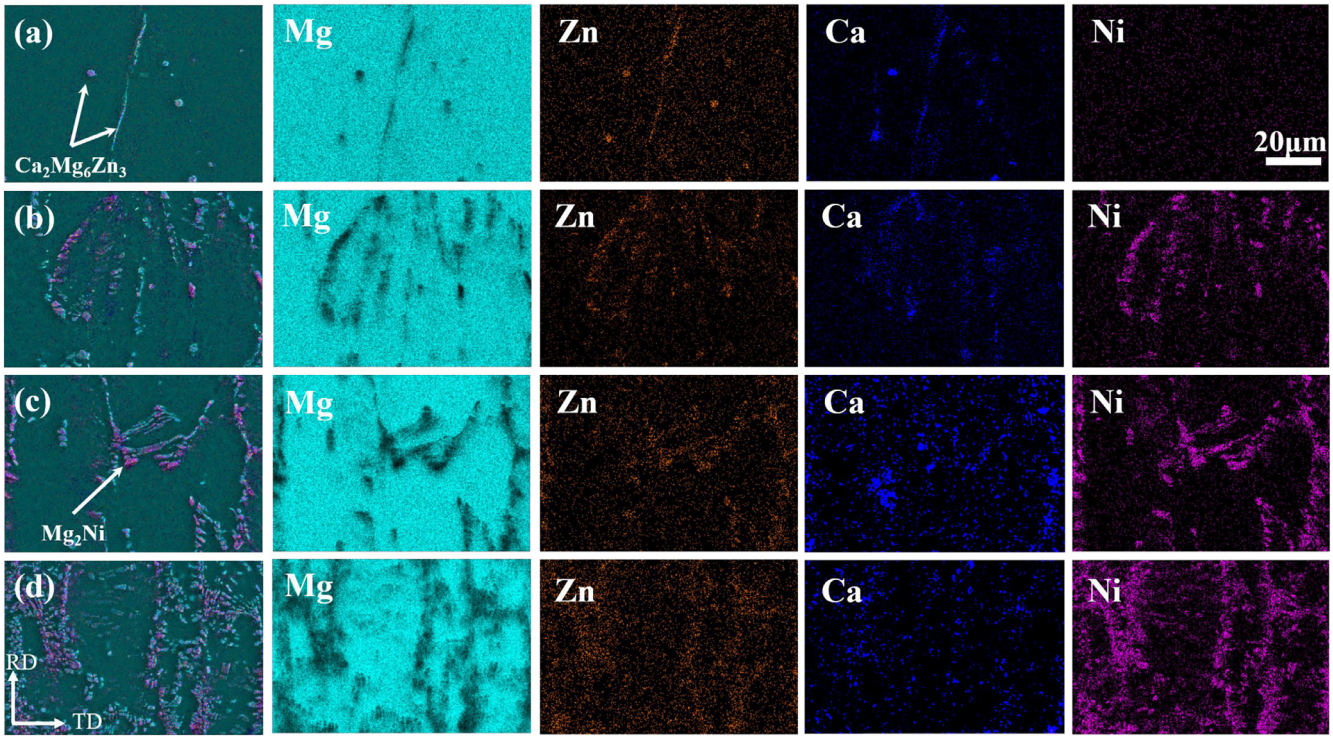

Fig. 5. EDS images of rolled Mg-1.5Zn-0.2Ca-xNi ($0 \leq x \leq 5$) alloys: (a) $x = 0$, (b) $x = 1$, (c) $x = 3$, (d) $x = 5$.

Table 3
Fitting results of EIS and Tafel plots and summary of corrosion rate at 25 °C.

Sample	R_s ($\Omega \cdot cm^2$)	R_{ct} ($\Omega \cdot cm^2$)	CPE_{dl}-T ($\mu F \cdot cm^{-2} \cdot s^{n-1}$)	CPE_{dl}-P ($0 \sim 1$)	E_{corr} (V vs SCE)	I_{corr} (mA cm^{-2})	C_{dl} (μF cm^{-2})	P_i (**mm y^{-1}**)	P_H (mm y^{-1})	P_W (mm y^{-1})
T6-0Ni	5.8 ± 0.1	693.7 ± 10.4	23±1	0.93±0.01	−1.51	0.035	12±1	1	9	15
T6-0.5Ni	6.3 ± 0.1	71.7 ± 0.7	200±4	0.88±0.01	−1.46	0.147	80±6	3	10	20
T6-1Ni	6.6 ± 0.1	73.4 ± 0.9	245±5	0.9 ± 0.01	−1.44	0.195	119±9	4	47	63
T6-2Ni	7.5 ± 0.1	23.8 ± 3.6	340±4	0.9 ± 0.01	−1.38	0.688	170±8	16	120	142
T6-3Ni	7.3 ± 0.1	8.3 ± 0.1	196±3	0.93±0.01	−1.30	0.845	114±6	19	261	311
T6-5Ni	7.6 ± 0.1	3.6 ± 0.1	382±1	0.87±0.01	−1.44	1.369	135±12	31	931	1436
R-0Ni	14.8 ± 0.1	519.6 ± 6.7	92±1	0.94±0.01	−1.52	0.410	60±2	9	9	13
R-1Ni	11.7 ± 0.1	4.2 ± 0.1	195±3	0.99±0.01	−1.38	0.848	181±11	19	664	706
R-3Ni	11.9 ± 0.1	2.8 ± 0.1	216±1	0.98±0.01	−1.32	1.050	185±16	24	996	1378
R-5Ni	12.1 ± 0.1	1.8 ± 0.1	529±2	0.87±0.02	−1.22	2.833	183±38	65	1471	1730

deviates from the linear relationship. The deviation might be due to the increase of electrochemistry active area or corrosion penetration.

After immersion for 30 min and achieving a steady state, EIS was applied to study the corrosion behavior of Mg-Zn-Ca-xNi ($0 \leq x \leq 5$) alloys at room temperature (Fig. 9). Only an intercept at high frequency range and a semi-circle at middle frequency range are observed. Correspondingly, the equivalent circuit $R_s(R_{ct}CPE_{dl})$ was used to fit the EIS plot (Fig. 9i) [38]. Wherein, R_s represents solution resistance, R_{ct} indicates charge transfer resistance for Mg dissolution, and CPE_{dl} indexes the Helmholtz double layer between NaCl solution and alloy [39,40]. The contribution of surface film could not be differentiated in EIS plots, indicating the corrosion products might be porous and un-protective. The fitting curves are given in Fig. 9a, d, and the fitting results are listed in Table 3. For Mg-Zn-Ca-xNi ($0 \leq x \leq 5$) alloys, the R_{ct} decreases significantly with Ni addition, inferring the dramatic effects of Ni on accelerating the electrochemical reaction. Intriguingly, C_{dl} increases with Ni content, suggesting a greater electrochemically active area or corrosion area [38,41]. It should mention that rolled Mg-1.5Zn-0.2Ca-xNi ($0 \leq x \leq 5$) alloys always exhibit a smaller R_{ct} than T6 Mg-12Zn-0.5Ca-xNi ($0 \leq x \leq 5$) alloys at the same Ni content. The low charge transfer resistance demonstrates a fast electrochemical reaction and poor corrosion resistance [12,42,43].

The Bode plots are regarded as useful tools for deeply understanding the electrochemical behaviors of the alloys [19]. The peaks observed in phase angle versus frequency plots signify the capacitor loop. Commonly, a higher peak of phase angle and a wider full width at half maximum (FWHM) indicate superior corrosion resistance of the alloy. Notably, as

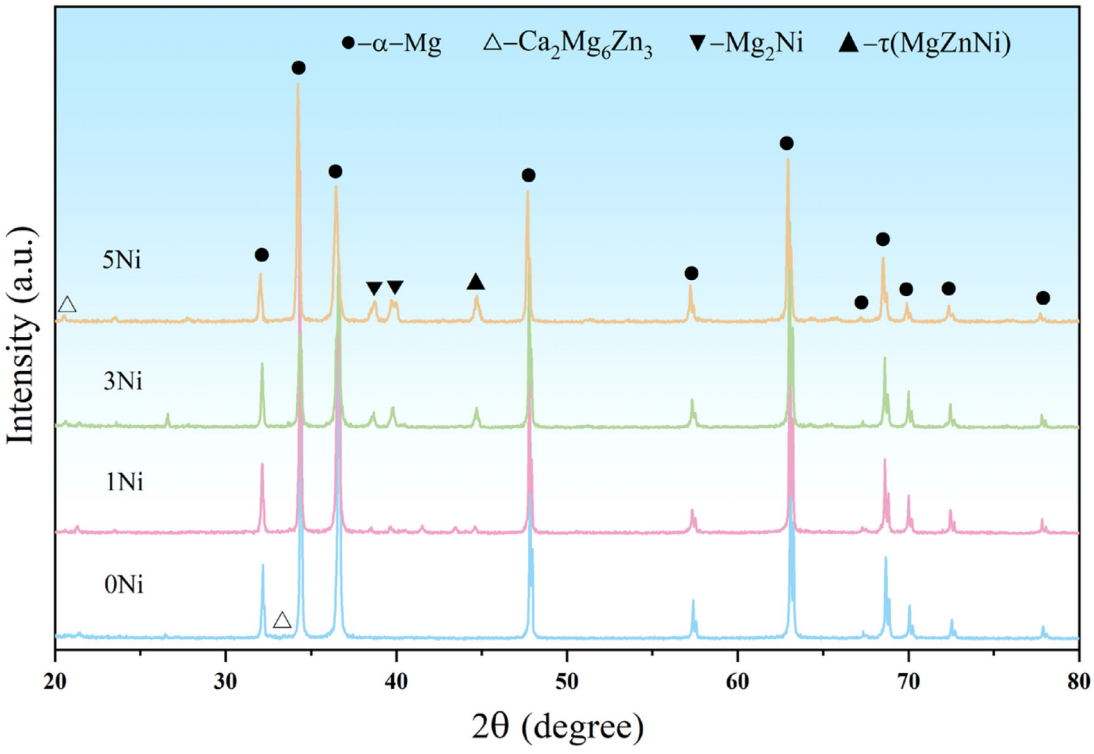

Fig. 6. XRD patterns of rolled Mg-1.5Zn-0.2Ca-xNi ($0 \leq x \leq 5$) alloys.

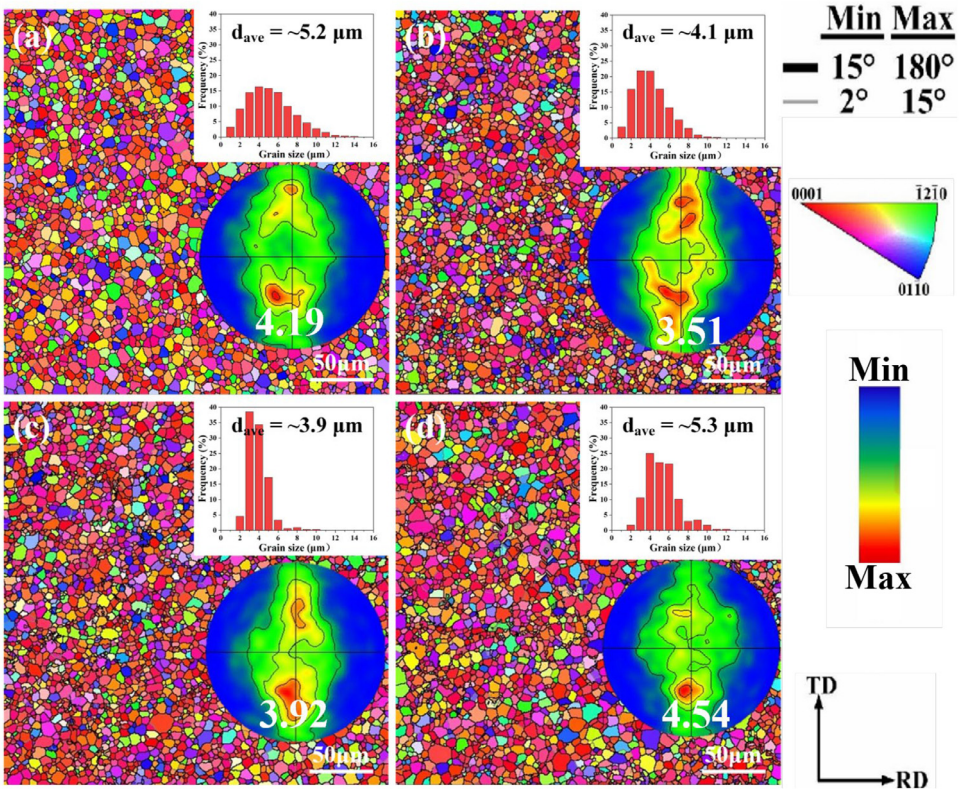

Fig. 7. EBSD inverse pole diagram (IPF) of rolled Mg-1.5Zn-0.2Ca-xNi ($0 \leq x \leq 5$) alloys: (a) $x = 0$, (b) $x = 1$, (c) $x = 3$, (d) $x = 5$. The insets present the corresponding grain distribution histogram and {0001} pole diagram.

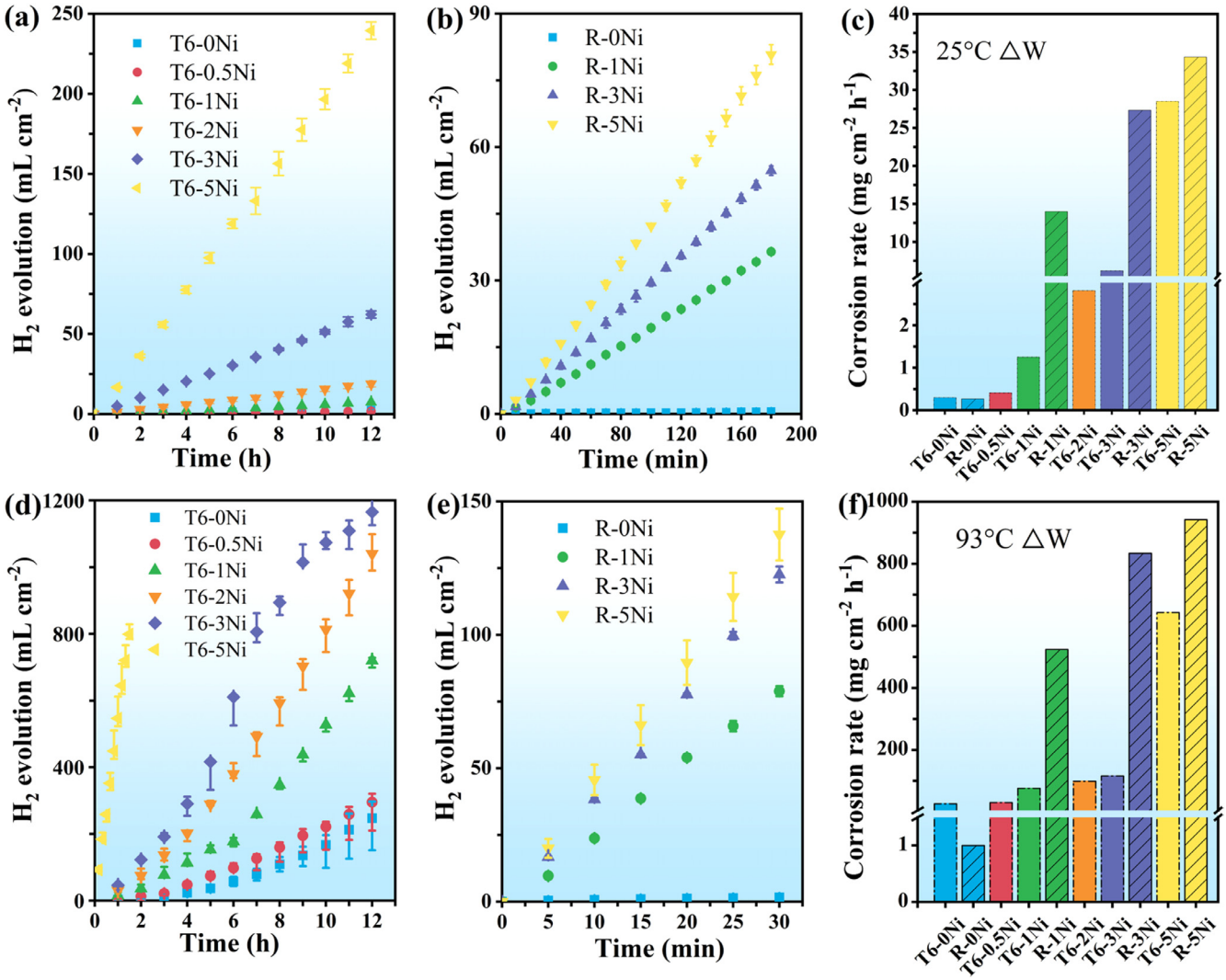

Fig. 8. Corrosion properties of Mg-Zn-Ca-xNi ($0 \leq x \leq 5$) alloys immersed in 3.5 wt.% NaCl solution at 25 °C & 93 °C: (a, b) H_2 evolution curves, and (c) corrosion rates tested from weight loss during immersion at 25 °C; (d, e) H_2 evolution curves, and (f) corrosion rates tested from weight loss during immersion at 93 °C.

Ni content increases, the peak of phase angle and FWHM exhibit a corresponding decrease, as evident in Fig. 9b and e. Furthermore, the impedance modulus (|Z|) also decreases with the increasing Ni content, as depicted in Fig. 9c and f. These phenomena indicate a rise in corrosion rates with the increased Ni content, aligning with the analysis of Nyquist plots.

DC polarization was employed after EIS test, to investigate the reaction kinetics, cathodic H_2 evolution, and anodic dissolution processes (Fig. 9g, h). It is evident that both the corrosion potential and corrosion current density increase with the incremental Ni content. The increased corrosion potential might be attributed to the larger fraction of noble MgZnNi and/or Mg_2Ni phase [18]. In addition, the cathodic H_2 evolution increases with the incremental Ni content, which should be the major reason for the increased corrosion current density. In contrast, the current density corresponding to anodic dissolution exhibits a negligible change.

Although the P_i, P_H and P_W exhibit a same trend, their values are hugely different, i.e., $P_i << P_H < P_W$. The significant deviation of P_i from P_H and P_W might be due to the serious peeling off of Mg particles from the matrix, which could not be counted by electrochemical test. The higher Ni content or larger corrosion rate could cause more severe peeling off of Mg particles, yielding a larger deviation. In addition, the complex reaction process evolved during polarization process would make the P_i underestimate the corrosion rate. Due to the existence of significant amount of second phases in Mg matrix and their electrochemical sluggishness, the P_H value is quite smaller than P_W. Moreover, as the second phases in T6 Mg-12Zn-0.5Ni-xNi ($0 \leq x \leq 5$) alloys perform a semi-closed skeleton, their peeling off should be alleviated compared to the separated second particles in rolled Mg-1.5Zn-0.2Ni-xNi ($0 \leq x \leq 5$) alloys. Therefore, the deviation between P_H and P_W is smaller in T6 Mg-12Zn-0.5Ni-xNi ($0 \leq x \leq 5$) alloys compared to rolled Mg-1.5Zn-0.2Ni-xNi ($0 \leq x \leq 5$) alloys.

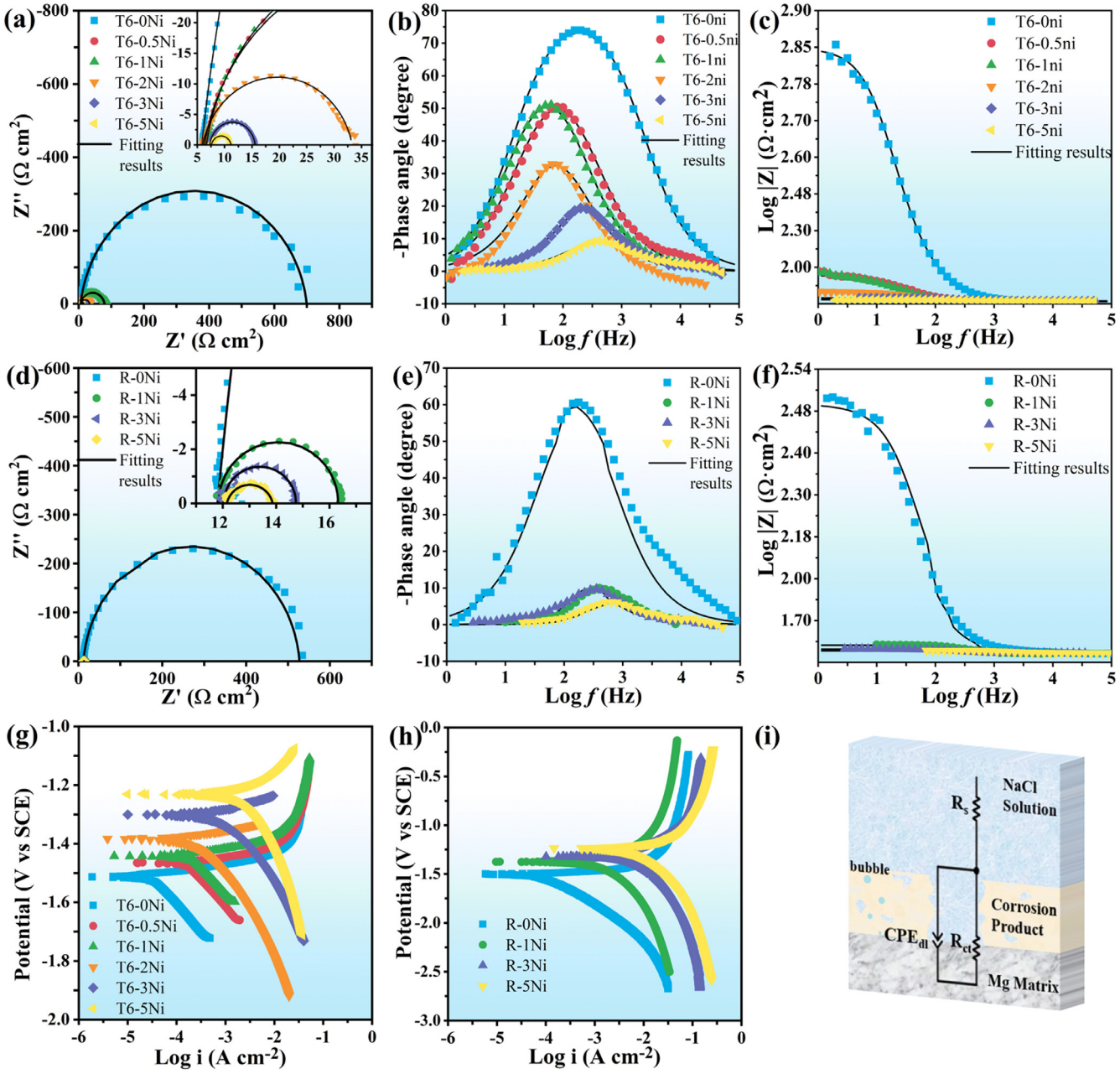

Fig. 9. EIS results of Mg-Zn-Ca-xNi ($0 \leq x \leq 5$) alloys immersed in 3.5 wt.% NaCl solution at 25 °C. (a, d) Nyquist plots, (b, c, e, f) Bode impedance plots and Bode phase angle plots, (g, h) Tafel curves, (i) the equivalent circuit.

Herein, both P_H and Pi underestimate the corrosion rate, and P_W is used to evaluate the corrosion properties of investigated alloys. The maximum corrosion rates are ~29 and ~34 mg cm^{-2} h^{-1} at 25 °C, and ~643 and ~942 mg cm^{-2} h^{-1} at 93 °C for T6 Mg-12Zn-0.5Ca-xNi ($0 \leq x \leq 5$) and rolled Mg-1.5Zn-0.2Ca-xNi ($0 \leq x \leq 5$) alloys, respectively.

Micro-galvanic corrosion is reckoned to be the main cause of corrosion in Mg alloys. Its severity is directly proportional to the magnitude of the Volta potential difference (VPD) between the intermetallic phase and α-Mg matrix. Thus, SKPFM was employed to measure the VPD between Mg matrix and second phases, as shown in Fig. 10. The intricate composition of the second phase makes it difficult to assign the potential peaks. As shown in Fig. 2 and 5, $Ca_2Mg_6Zn_3$ and MgZnNi are the primary constituent phase in Ni-free and Ni-containing alloys respectively. Consequently, the VPD in T6 Mg-12Zn-0.5Ca and rolled Mg-1.5Zn-0.2Ca alloys should be assigned to the value between $Ca_2Mg_6Zn_3$ and α-Mg matrix. Similarly, the VPD in T6 Mg-12Zn-0.5Ca-3Ni and rolled Mg-1.5Zn-0.2Ca-3Ni alloys should be assigned to the value between MgZnNi and α-Mg matrix. According to the results shown in Fig. 10, the VPD value between Mg matrix and CaMgZn phase is approximately 150 mV, and the VPD value between Mg matrix and MgZnNi phase is about 300~350 mV

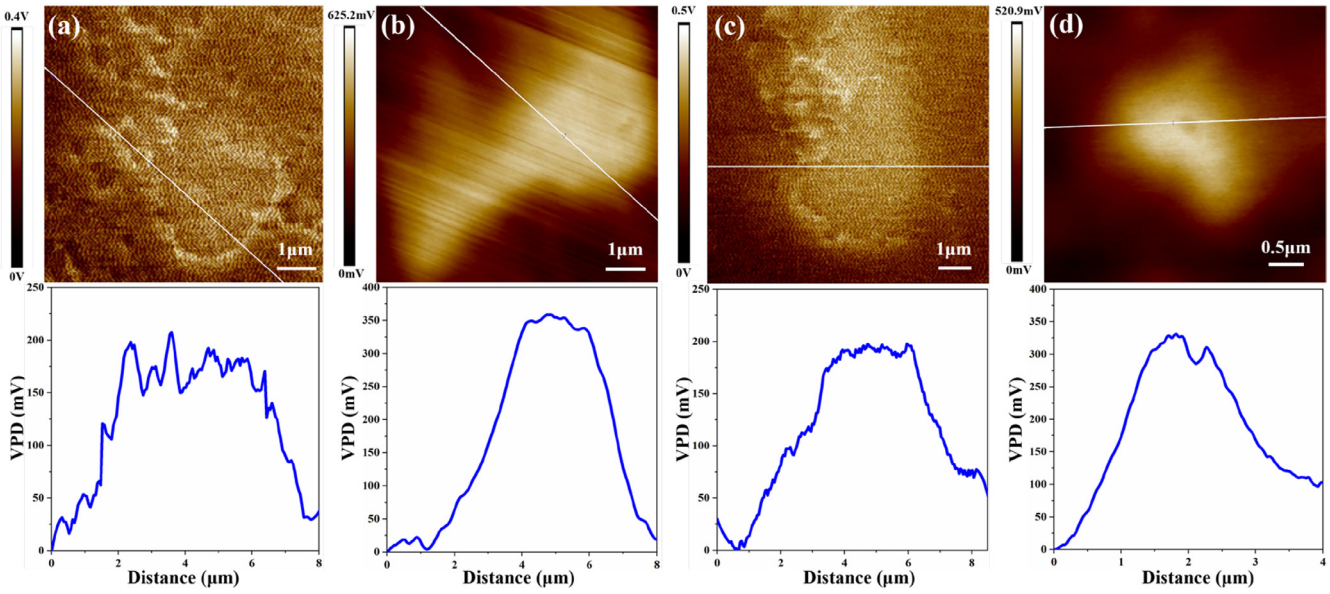

Fig. 10. Volta potential maps of the investigated alloys with Volta potential profiles along the lines in the maps: (a) T6 Mg-12Zn-0.5Ca, (b) T6 Mg-12Zn-0.5Ca-3Ni, (c) rolled Mg-1.5Zn-0.2Ca, (d) rolled Mg-1.5Zn-0.2Ca-3Ni alloys.

in T6 Mg-12Zn-0.5Ca-3Ni and rolled Mg-1.5Zn-0.2Ca-3Ni alloys, respectively. Furthermore, it is reasonable to believe that MgZnNi phase has a much higher Volta potential than that of MgZn phase. The dramatic increase of VPD between second phase and Mg matrix should have a determinant effect on corrosion behaviors.

Additionally, the surface morphology was characterized by both SEM and LSCM. Fig. 11 and 12 show the SEM images of corroded Mg-Zn-Ca-xNi ($0 \leq x \leq 5$) alloys with product film. Only 1-min immersion was conducted due to the high corrosion rate. Inhomogeneous corrosion occured, with obvious hump-like area and flat area. With the increase of Ni content, the humps increased, indicating more serious localized corrosion. The magnification of flat area revealed that it is constructed by loose stacked flakes (Fig. 11a-f, Fig. 12a-d). The magnification of serious corrosion area shows the corrosion film is turtle-shell like, where abundant chaps are spread all over. The chaps might be caused by H_2 evolution. EDS results show that the thick production area is rich in O element, corresponding to the metal oxide and/or metal hydroxide. The turtle-shell like corrosion area is surround by Ni-rich and Zn-rich particles, indicating the galvanic-corrosion majors the corrosion process (Fig. 11a-f). For comparison, rolled Mg-1.5Zn-0.2Ca-xNi ($0 \leq x \leq 5$) exhibit a relatively homogeneous corrosion than T6 Mg-12Zn-0.5Ca-xNi ($0 \leq x \leq 5$), probably attributing to the smashed eutectic phases and their relatively homogeneous distribution.

The lateral profiles of corroded alloys were observed. The corrosion product film becomes thicker with the incremental Ni content, corresponding to the increased corrosion thickness. Most importantly, perforative cracks are observed in the corrosion product film. They allow the corrosion medium penetrate into α-Mg matrix, resulting in a poor or negligible protection of the corrosion product film. Intriguingly, the corrosion is blocked by the net-structured eutectic phases in T6 Mg-12Zn-0.5Ca-xNi ($0 \leq x \leq 5$) alloys, indicating the eutectic phase not only serves as a galvanic cathode but also functions as a corrosion barrier (Fig. 11h-m). In contrast, the isolated eutectic phase in Mg-1.5Zn-0.2Ca-xNi ($0 \leq x \leq 5$) could not block the corrosion penetration into the α-Mg matrix (Fig. 12e-h), they are imbedded in the corrosion product film when peeling off from the α-Mg matrix.

Corrosion morphology without corrosion product was characterized by SEM and LSCM (Fig. 13). As to T6 Mg-12Zn-0.5Ca-xNi ($0 \leq x \leq 5$) alloys, the corrosion occurs around the eutectic phase, and the dissolution of Mg matrix conversely yields the peeling off of eutectic phase from these alloys. It is more like a grain boundary corrosion. For rolled Mg-1.5Zn-0.2Ca-xNi ($0 \leq x \leq 5$) alloys, the isolated eutectic phases and refined grains yield a relatively homogeneous corrosion (Fig. 13g-j). Fig. 13 gives the macro corrosion morphology of Mg-Zn-Ca-xNi ($0 \leq x \leq 5$) alloys. With the increase of Ni content, the corrosion pits become larger and deeper, indicating the enhanced degradation rate, which is consistent with H_2 evolution and electrochemical results.

3.3. Mechanical properties of Mg-Zn-Ca-xNi ($0 \leq$ x ≤ 5) alloys

Mechanical property is another important factor for fracturing materials. Fig. 14 shows the mechanical curves of Mg-Zn-Ca-xNi ($0 \leq x \leq 5$) series alloys collected at room temperature, and the corresponding parameters, for example, yield strength (YS), ultimate tensile strength (UTS) and elongation to failure (EL) are summarized in Table 4. In addition, the work hardening θ/ε plots of Mg-Zn-Ca-xNi alloys are presented in Fig. 14c and d. In the case of T6 Mg-12Zn-0.5Ca-xNi series alloys, the YS exhibits

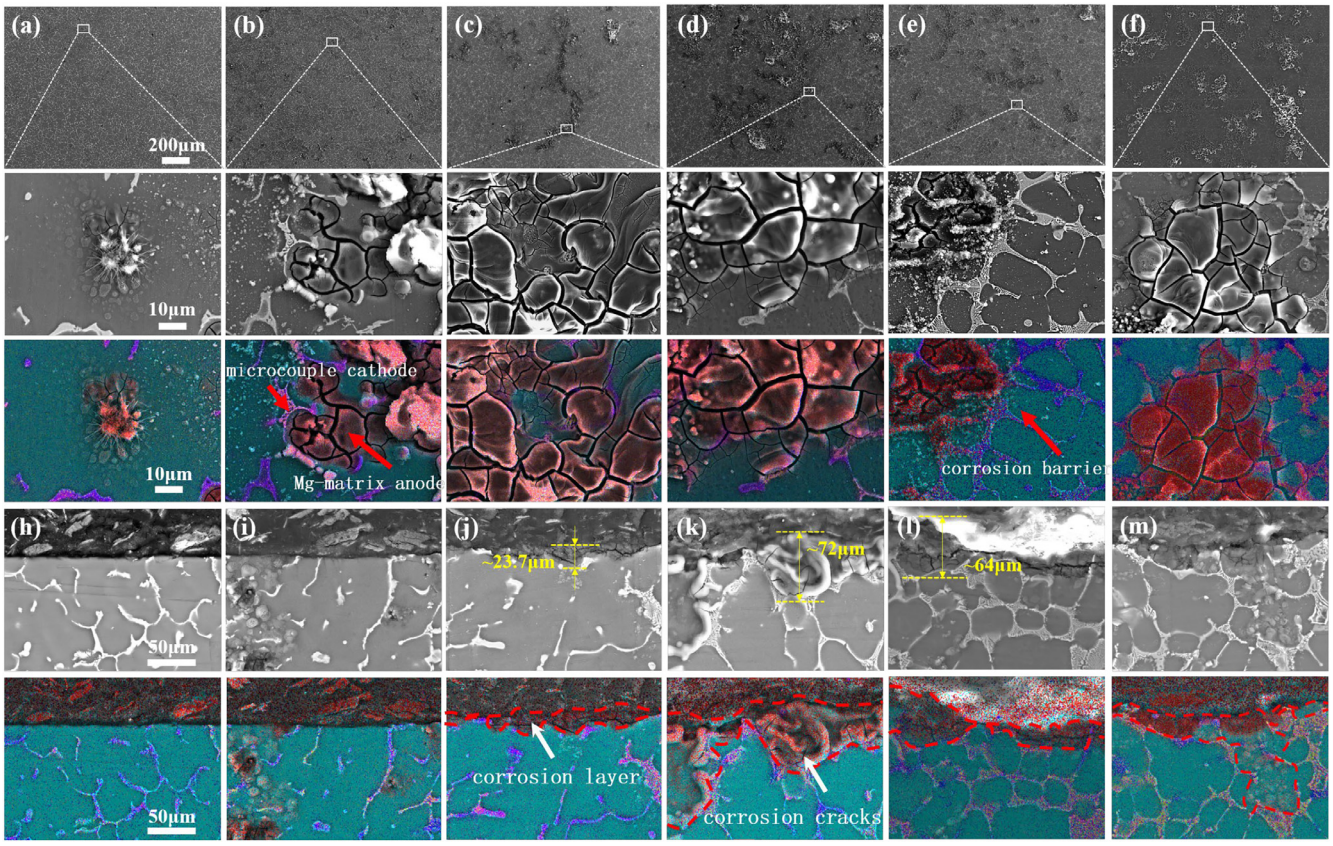

Fig. 11. Corrosion morphology of T6-Mg-12Zn-0.5Ca-xNi ($0 \leq x \leq 5$) alloys immersed in 3.5 wt.% NaCl solution for 1 min. (a-f) Surface morphology and (h-l) lateral profile of alloys with $x = 0$, 0.5, 1, 2, 3, 5, respectively.

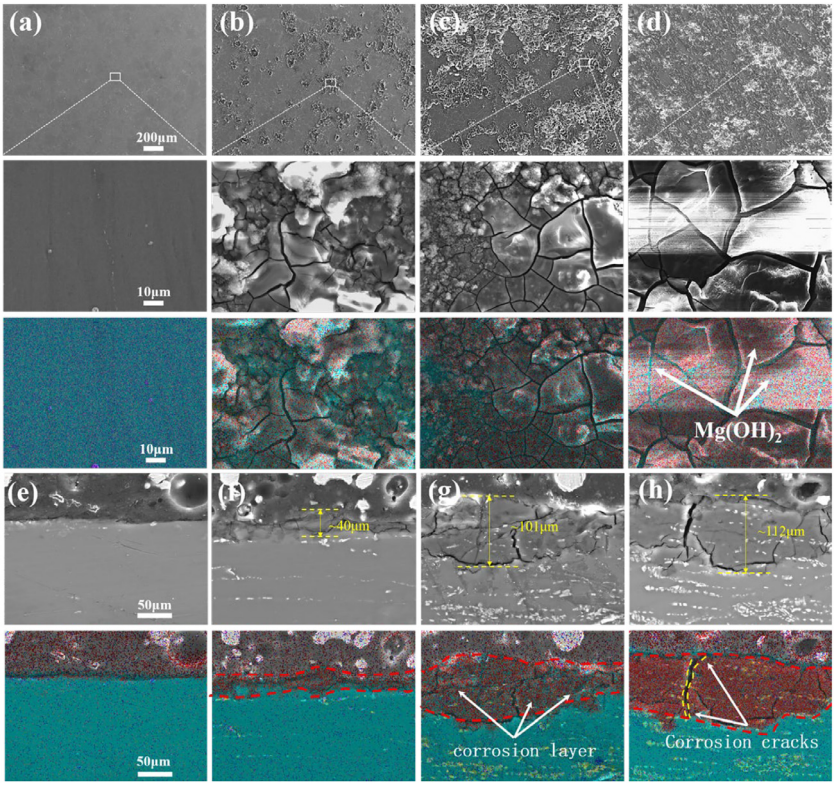

Fig. 12. Corrosion morphology of rolled Mg-1.5Zn-0.2Ca-xNi ($0 \leq x \leq 5$) alloys immersed in 3.5 wt.% NaCl solution for 1 min. (a-d) Surface morphology and (e-h) lateral profile of alloys with $x = 0$, 1, 3, 5, respectively.

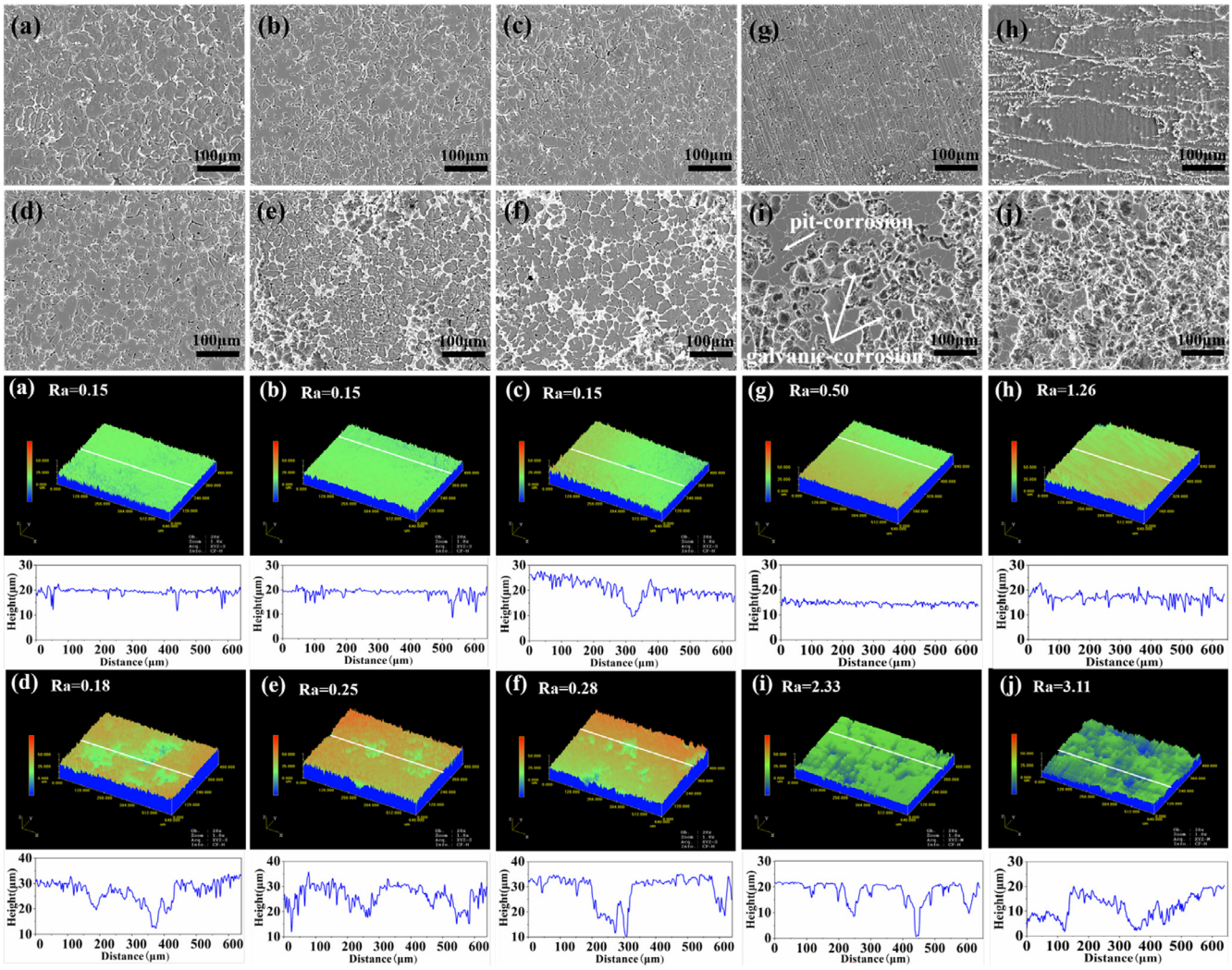

Fig. 13. Corrosion morphology and 3D corrosion morphologies of Mg-Zn-Ca-xNi ($0 \leq x \leq 5$) alloys: (a-f) T6 Mg-12Zn-0.5Ca-xNi ($0 \leq x \leq 5$) and (g-j) rolled Mg-1.5–0.2Ca-xNi ($0 \leq x \leq 5$) immersed in 3.5 wt.% NaCl solution after 1 min. The corrosion product was removed before characterization.

Table 4
Mechanical properties of Mg-Zn-Ca-xNi ($0 \leq x \leq 5$) alloys.

Composition (wt.%)	YS/MPa	UTS/MPa	EL (%)
T6 Mg-12Zn-0.5Ca-0Ni	156.9 ± 1.1	237.9 ± 1.8	8.2 ± 0.6
T6 Mg-12Zn-0.5Ca-0.5Ni	168.6 ± 1.4	240.3 ± 2.3	6.1 ± 1.1
T6 Mg-12Zn-0.5Ca-1Ni	144.3 ± 2.0	233.4 ± 1.9	6.5 ± 1.2
T6 Mg-12Zn-0.5Ca-2Ni	130.5 ± 1.2	225.3 ± 1.3	6.0 ± 1.0
T6 Mg-12Zn-0.5Ca-3Ni	130.9 ± 0.8	215.3 ± 1.4	4.8 ± 1.5
T6 Mg-12Zn-0.5Ca-5Ni	127.5 ± 2.1	190.0 ± 1.7	3.2 ± 1.3
Rolled Mg-1.5Zn-0.5Ca-0Ni	185.5 ± 2.3	239.3 ± 1.2	26.5 ± 2.1
Rolled Mg-1.5Zn-0.2Ca-1Ni	188.0 ± 0.9	233.1 ± 1.0	17.3 ± 2.5
Rolled Mg-1.5Zn-0.2Ca-3Ni	195.5 ± 1.3	242.6 ± 2.3	16.0 ± 1.5
Rolled Mg-1.5Zn-0.2Ca-5Ni	185.4 ± 0.8	221.7 ± 2.5	8.1 ± 1.8

a parabolic trend against Ni content, and reaches high maximum value of 168.6 ± 1.4 MPa. The further addition of Ni could decrease the YS continuously. Similar to the trend of YS, the UTS shows the maximum value of 240.3 ± 2.3 MPa when 0.5 wt.% Ni addition. Moreover, the EL decreases gradually with the Ni content, which is attributed to the occurrence of early fracture induced by larger eutectic particles (Fig. 1).

In terms of rolled Mg-1.5Zn-0.2Ca-xNi alloys, both the YS and UTS perform a parabolic trend, with maximum values of 195.5 ± 1.3 MPa and 221.7 ± 2.5 MPa at 3 wt.% Ni content. Meanwhile, the EL decreases monotonously from 26.5 ± 2.1% to 8.1 ± 1.8% with the addition of Ni up to 5 wt.% Ni (Table 4). Compared with T6 Mg-12Zn-0.5Ca-xNi alloys, rolled Mg-1.5Zn-0.2Ca-xNi alloys exhibit a superior combination of strengths and ductility, *i.e.*, both higher YS (>180 MPa) and EL (>15%). Especially, 3 wt.% Ni alloying demonstrates the most effective strengthening effect.

According to the work hardening curves (Fig. 14), T6 Mg-12Zn-0.5Ca-Ni alloys exhibit similar work hardening behaviors. Indeed, the work hardening rate of all six samples decreases with strains and maintains a stable state over 2%. Differently, rolled Mg-1.5Zn-0.2Ca-Ni alloys possess three deformation stages. The work hardening rate decreases rapidly at the initial stage, followed by an increment of work hardening rate. At the last stage, the work hardening rate linearly

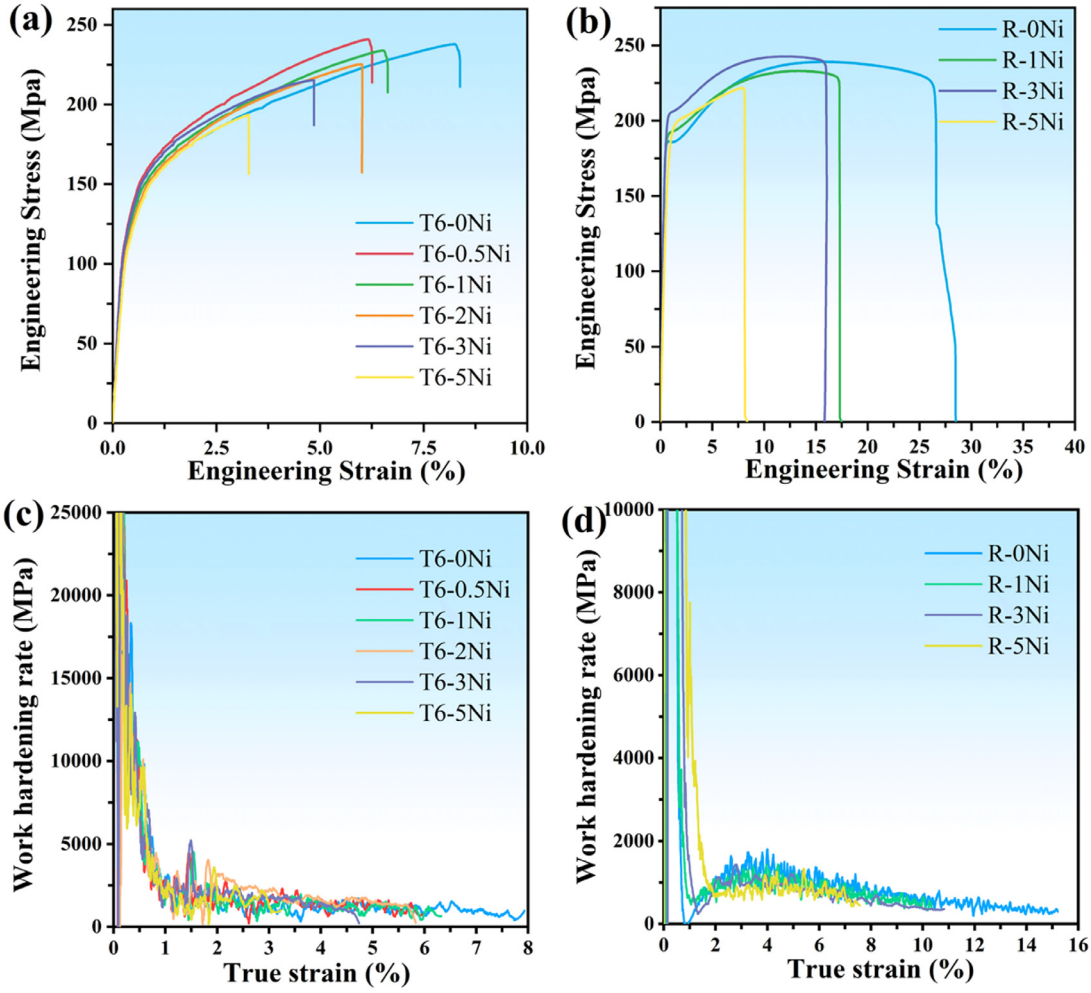

Fig. 14. Room-temperature engineering tensile strain-stress curves and corresponding work hardening curves: (a, c) T6 Mg-12Zn-0.5Ca-xNi ($0 \leq x \leq 5$) and (b, d) rolled Mg-1.5Zn-0.2Ca-xNi ($0 \leq x \leq 5$) alloys.

decreases for strains over 4%. The greater work hardening ability of rolled Mg-1.5Zn-0.2Ca alloy can be responsible for the better combination of strengths and ductility.

To accurately replicate the realistic operational conditions for fracturing materials during gas/oil exploration, the temperature of the mechanical test was precisely set at 93 °C (Fig. S2, Table S1). It is evident that both yield strength (YS) and ultimate tensile strength (UTS) are decreased compared to their values at room temperature, attributing to the coarsening of grains during tension at higher temperatures [44]. Meanwhile, the elongation to failure is improved compared to their values at room temperature. It is well known that the activation of non-basal slip is responsible for the enhanced ductility at moderate temperature, owing to the decreased critical resolved shear stress (CRSS) of non-basal slip at elevated temperature [45].

4. Discussion

In short, the adjustable mechanical properties and degradation rate were achieved via composition tuning and deformation processing. The corresponding results are summarized in Fig. 15 [17,21,26,46-48]. The parabola-like mechanical properties and exponential increasing corrosion rate with Ni content indicate the Ni alloying has a more dramatic effect on corrosion rather than mechanical properties, and a higher corrosion rate could be obtained at a remunerative cost of mechanical properties, depending on the practical requirement of degradable materials. In addition, Mg-Zn-Ca-xNi ($0 \leq x \leq 5$) alloys exhibit higher corrosion rates compared to the alloys reported in previous studies, a comparable or even higher UTS compared with the reported RE-free alloys, but a lower UTS compared with the reported RE-containing alloys.

4.1. Corrosion mechanism

Based on EIS and SEM analyses, the presence of perforative cracks in the corrosion product films of Mg-Zn-Ca-xNi ($0 \leq x \leq 5$) alloys has minimal impact on their corrosion behavior. These cracks are likely caused by the vigorous release of H_2 gas during immersion. Consequently, the microstructure, including the second phases and grain size, takes precedence in influencing the corrosion properties.

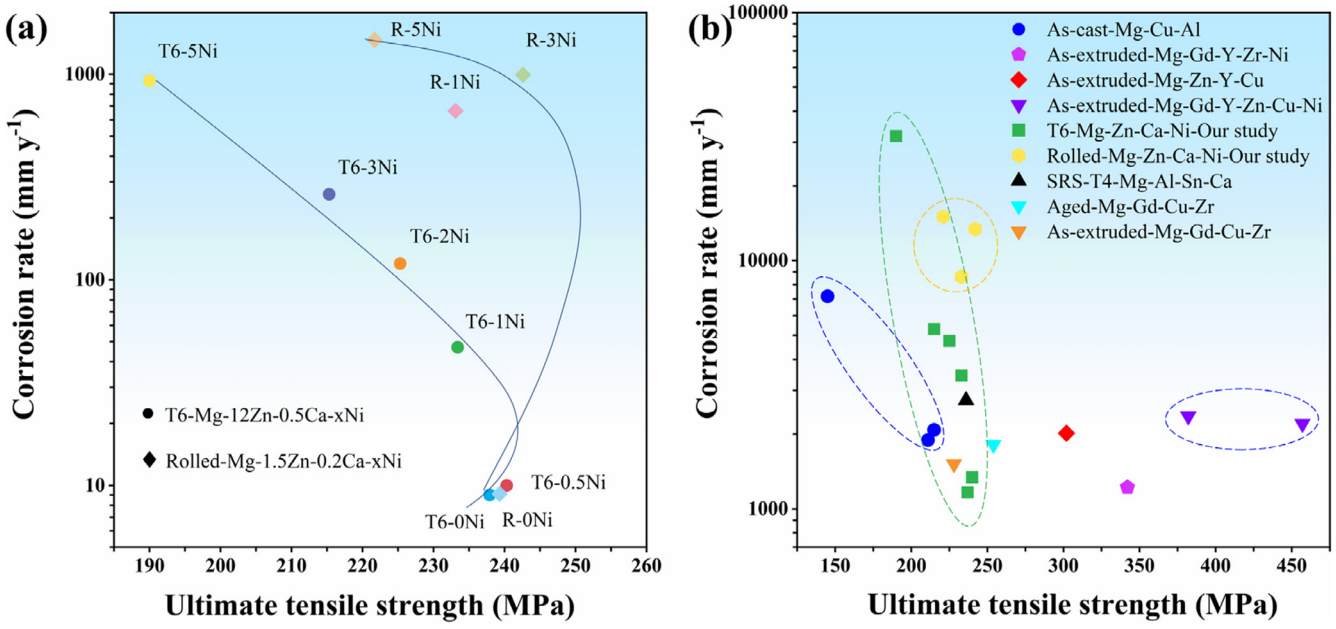

Fig. 15. Illustration of mechanical properties and corrosion rate of Mg-Zn-Ca-xNi ($0 \leq x \leq 5$) alloys. (a) Corrosion rate *vs* ultimate tensile strength at 25 °C, (b) comparison of ultimate tensile strength at 25 °C and corrosion rate at 93 °C with literatures.

4.1.1. The effects of the secondary phase

The second phase exerts contrasting influences on the corrosion process. In Ni-free alloys, the T6 Mg-12Zn-0.5Ca alloy exhibits a semi-closed network comprising significant quantities of Mg_7Zn_3, $MgZn_2$, Mg_2Zn_3, and $Ca_2Mg_6Zn_3$ phases. Conversely, the rolled Mg-1.5Zn-0.2Ca alloy displays a sparse and random distribution of $Ca_2Mg_6Zn_3$ particles. Despite these notable differences in the second phase, both alloys demonstrate a comparable corrosion rate of approximately 9 mm y^{-1}. While the increased presence of Mg_7Zn_3, $MgZn_2$, Mg_2Zn_3, and $Ca_2Mg_6Zn_3$ phases in the T6 alloy enhance galvanic corrosion by multiplying galvanic couples, the continuous network distribution of these phases can serve as a corrosion barrier, slowing down the corrosion process. The opposing contributions of these factors balance out, leading to a similar corrosion rate for both alloys, as illustrated in Fig. 16a and c.

The addition of Ni elevates the Volta potential difference (VPD) between the second phase and α-Mg matrix, thereby augmenting the cathodic H_2 evolution process. As the Ni content increases in T6 Mg-12Zn-0.5Ca-xNi ($0 \leq x \leq 5$) alloys, the corrosion rate also rises due to the proliferation of noble second phases. This phenomenon indicates that the Ni-containing eutectic phases play a dominant role in enhancing galvanic corrosion compared to their ability to serve as corrosion barriers (Fig. 16b). Conversely, in rolled Mg-1.5Zn-0.2Ca-xNi ($0 \leq x \leq 5$) alloys, the network structure is disrupted, eliminating their corrosion barrier effects (Fig. 16d). The heightened galvanic potential and the increased number of galvanic couples, both attributed to Ni alloying, lead to an even higher corrosion rate compared to T6 Mg-12Zn-0.5Ca-xNi ($0 \leq x \leq 5$) alloys with the same Ni content (Fig. 16b, d).

4.1.2. The effects of grain size

Furthermore, grain size also influences the corrosion rate. Recent studies revealed a relationship between corrosion current density and grain size, which is akin to the Hall-Petch relationship [49-54]. For high-purity metals experiencing uniform corrosion, the relationship between uniform corrosion current (i_{uc}) and mean grain size ($\bar{d}$) can be expressed as follows:

$$i_{uc} = \alpha + b(\bar{d})^{-\frac{1}{2}} \times e^{-\frac{9}{8}S_n^2} \quad (5)$$

Where α and b are constants that vary from materials and corrosive environments, S_n represents the standard deviation of number-weighted grain size distribution. The corrosion resistance improves with the increase of grain size in a non-passivating environment ($\alpha < 0$, $b > 0$), while it shows an opposite behavior in a passivating environment ($\alpha > 0$, $b < 0$). Obviously, it should be a non-passivating environment in our work, and the corrosion rate should increase as the grain size decreases. Therefore, the decreased grain size contributes to the increased corrosion rate for rolled Mg-1.5Zn–0.2Ca-xNi ($0 \leq x \leq 5$) alloys compared to T6 Mg-12Zn-0.5Ca-xNi ($0 \leq x \leq 5$) alloys. It also contributes to the increased corrosion rate of rolled Mg-1.5Zn–0.2Ca-xNi ($0 \leq x \leq 5$) alloys with higher Ni content, as the grain size decrease from 5.3 to 3.9 μm. However, due to the complexity of the corrosion environment, assignment of α, b and S_n is difficult. Consequently, it is difficult to quantify the effect of grain size on corrosion.

4.2. Mechanical properties

The addition of Ni has a significant impact on the YS. For the low-Zn alloys, the YS of rolled Ni-free alloy is

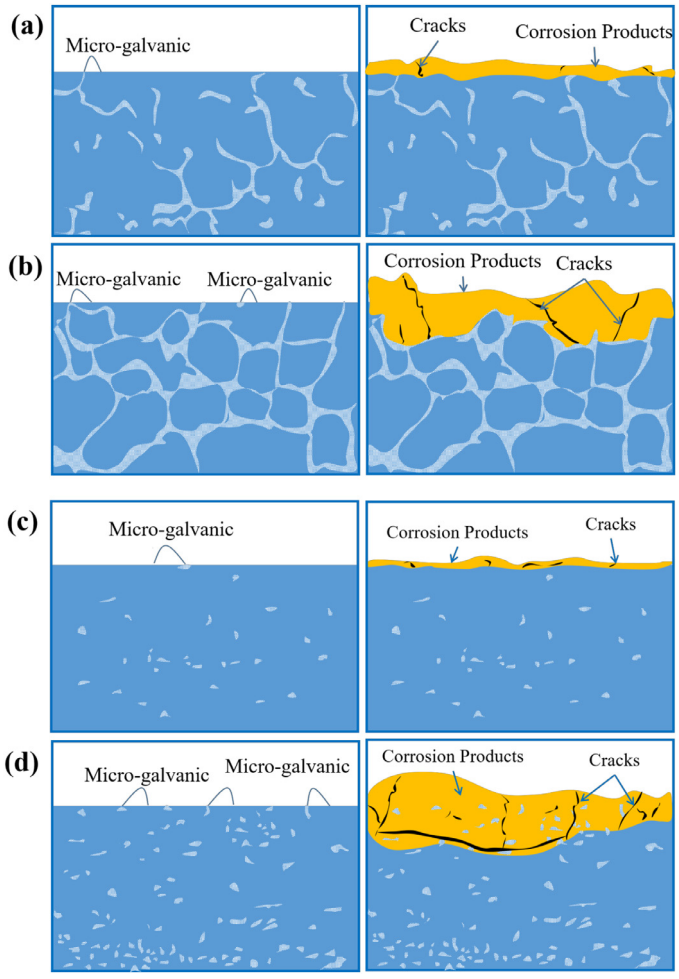

Fig. 16. Corrosion mechanism of Mg-Zn-Ca-xNi ($0 \leq x \leq 5$) alloys. (a) Counter balanced galvanic corrosion and corrosion barrier effect of network-like eutectic phases in T6-Mg-12Zn-0.5Ca alloy. (b) Intensified and multiplied galvanic couples overwhelm the corrosion barrier effect, boosting the corrosion rate of T6 Mg-12Zn-0.5Ca-xNi alloys. (c) Weak galvanic corrosion and low barrier effect in rolled Mg-1.5Zn-0.2Ca alloy. (d) Intensified and multiplied galvanic couples boost the corrosion rate of rolled Mg-1.5Zn-0.2Ca-xNi alloys.

185.5 ± 2.3 MPa (Table 4). Moreover, when 1 wt.% Ni is added, the YS increases to 188.0 ± 0.9 MPa. This increment becomes more significant with the addition of 3 wt.% Ni, reaching a remarkable value of 195.5 ± 1.3 MPa. The YS can be described as follows:

$$\Delta\sigma_y = \Delta\sigma_{GB} + \Delta\sigma_{ss} + \Delta\sigma_{ppt} \quad (6)$$

Where $\Delta\sigma_{GB}$, $\Delta\sigma_{ss}$ and $\Delta\sigma_{ppt}$ represent grain boundary strengthening, solid solution strengthening and precipitation strengthening, respectively.

According to our recent studies [55-57], grain boundary strengthening plays a prominent role in determining the YS. The contribution of $\Delta\sigma_{GB}$ can be calculated by Hall-Petch relation [58]:

$$\Delta\sigma_{gb} = k/d^{1/2} \quad (7)$$

Where k is the Hall-Petch slope and d is the average grain size. The value of k is selected as 209 MPa $\mu m^{-1/2}$ for rolled Mg alloys. With increasing Ni content from 0 to 1 wt.% and then to 3 wt.%, the average grain size of rolled alloys decreases from 5.2 μm to 4.1 μm and further to 3.9 μm (Fig. 7), respectively. Substituting above data, $\Delta\sigma_{GB}$ can be figured out as 14 MPa for 3 wt.% Ni addition, compared with Ni-free alloy.

In Mg-1.5Zn-0.2Ca-xNi alloys, the effect of precipitation strengthening is limited due to the micro-sized second phases (Fig. 4). Although the Ni content is relatively high, at 1, 3, 5 wt.%, the total Ni solutes in the matrix is limited, due to the formation of large $Ca_2Mg_6Zn_3$ phase covered by Mg_2Ni phase (Fig. 5). Consequently, increasing Ni content provides a negligible contribution to the enhanced solution strengthening. Summarizing all data above, the calculated increment in YS after the addition of 3 wt.% Ni is approximately 14 MPa, which closely matches the experimental value of approximately 10 MPa. It suggests that the improved grain boundary strengthening is primarily responsible for the higher YS of Mg-1.5Zn-0.2Ca-3Ni alloy.

A small amount of Ni can increase the strength of the alloy, but also reduce its to plasticity due to the formation of Mg_2Ni phase [19]. In this work, excessive Ni addition leads to an increase of micro-scale secondary phase, which acts as nucleation site for microcracks and promote a more brittle fracture tendency. The maximum ultimate tensile strength is achieved at $x = 3$, with a value of 242.6 MPa.

5. Conclusion

In the present work, the microstructure, corrosion behavior and mechanical properties and of Mg-Zn-Ca-xNi ($0 \leq x \leq 5$) alloys were studied, so as to achieve the adjustable mechanical and corrosion properties for fracturing materials. The main conclusions are as follows:

(1) In the high-zinc as-cast Mg-12Zn-0.5Ca alloys, the addition of Ni induces the formation of un-stoichiometric MgZnNi phases and Mg_2Ni phase, which is dependent on the Ni content. Homogenization and ageing treatment do not change the eutectic phase significantly. The low-zinc rolled Mg-1.5Zn-0.2Ca-xNi alloys exhibit a fewer second phases, which are randomly distributed in α-Mg matrix.

(2) In T6-Mg-12Zn-0.5Ca-xNi alloys, the presence of network-like Ni-containing eutectic phases enhances the galvanic couples, overwhelming their corrosion barrier effects and boosting the corrosion rate significantly. Hot-rolling disrupts the network-like second phases, leading to an even higher corrosion rate for the Mg-1.5Zn-0.2Ca-xNi alloys. The maximum corrosion rates are 29 and 34 mg cm^{-2} h^{-1} at 25 °C, and 643 and 942 mg cm^{-2} h^{-1} at 93 °C for T6 Mg-12Zn-0.5Ca-xNi and rolled Mg-1.5Zn-0.2Ca-xNi alloys, respectively.

(3) High-zinc T6 Mg-12Zn-0.5Ca-xNi alloys feature a simple and short manufacturing process, making them suitable for the use in fracturing balls. In contrast, the low-zinc rolled Mg-1.5Zn-0.2Ca-xNi alloys exhibit ex-

cellent deformability, making them feasible for use in fracturing rings in bridge plug. The adjustable mechanical properties and degradation rate of Mg-Zn-Ca-xNi ($0 \leq x \leq 5$) make them feasible for use in various components.

Declaration of competing interest

The authors declare that they have no known competing financial interests or personal relationships that could have appeared to influence the work reported in this paper.

CRediT authorship contribution statement

Dawei Wang: Writing – review & editing, Writing – original draft, Methodology, Investigation, Data curation, Conceptualization. **Xiangshuang Jiang:** Writing – review & editing. **Changxin Chen:** Investigation. **Xun Zhang:** Investigation. **Zhong-Zheng Jin:** Supervision, Conceptualization. **Fuyong Cao:** Data curation. **Jia-Ning Zhu:** Data curation. **Cheng Wang:** Writing – review & editing. **Yinlong Ma:** Writing – review & editing. **Min Zha:** Supervision, Conceptualization.

Acknowledgement

This work was primarily supported by the National Key Research and Development Program (No. 2022YFE0122000) and National Natural Science Foundation of China under Grant Nos. 52234009, 52274383, 52222409, and 52201113. Partial financial support came from the Fundamental Research Funds for the Central Universities, JLU, Program for JLU.

Supplementary materials

Supplementary material associated with this article can be found, in the online version, at doi:10.1016/j.jma.2024.07.011.

References

[1] C. Franco, R. Solares, H. Marri, H. Hussain, The use of stagefrac new technology to complete and stimulate horizontal wells: field case, 2008 https://doi.org/10.2118/120806-MS.
[2] D. Themig, J. Petroleum Technol. 63 (2011) 26–31, doi:10.2118/0411-0026-jpt.
[3] D.R. Watson, D.G. Durst, J.T. Harris and J.D. Contreras, One-Trip Multistage Completion Technology for Unconventional Gas Formations, Society of Petroleum Engineers https://doi.org/10.2118/114973-MS.
[4] Z. Xu, G. Agrawal, B.J. Salinas, Smart nanostructured materials deliver high reliability completion tools for gas shale fracturing, 2011. https://doi.org/10.2118/146586-MS.
[5] X. Pei, S. Wei, B. Shi, Z. Shen, X. Wang, Z. Tong, T. Fu, Pet. Explor. Dev. 41 (2014) 805–809, doi:10.1016/s1876-3804(14)60097-5.
[6] C. Zheng, Y.H. Liu, H.X. Wang, C. Chen, J. Qin, Z.K. Liu, Y. Shen, J. Nat. Gas Sci. Eng. 34 (2016) 401–411, doi:10.1016/j.jngse.2016.07.008.
[7] I. Aviles, M. Dardis, M. Marya, Journal of Petroleum Technology 65 (2013) 32–33, doi:10.2118/1113-0032-JPT.
[8] B.J. Salinas, Z. Xu, G. Agrawal, B.M. Richard, Controlled electrolytic metallics - an interventionless nanostructured platform, SPE International Oilfield Nanotechnology Conference and Exhibition, 2012.
[9] T. Bu, R. Jia, T. Ying, A. Atrens, P. Chen, D. Zheng, F. Cao, Acta Metallurgica Sinica (English Letters) 36 (2023) 1630–1648, doi:10.1007/s40195-023-01582-z.
[10] F. Cao, B. Xiao, Z. Wang, T. Ying, D. Zheng, A. Atrens, G.-L. Song, J. Magnesium Alloys 11 (2023) 2084–2095, doi:10.1016/j.jma.2021.08.024.
[11] S. Pawar, T.J.A. Slater, T.L. Burnett, X. Zhou, G.M. Scamans, Z. Fan, G.E. Thompson, P.J. Withers, Acta Mater. 133 (2017) 90–99, doi:10.1016/j.actamat.2017.05.027.
[12] P.-p. Wu, F.-j. Xu, K.-k. Deng, F.-y. Han, Z.-z. Zhang, R. Gao, Corros. Sci. 127 (2017) 280–290, doi:10.1016/j.corsci.2017.08.014.
[13] S. Wang, H. Pan, D. Xie, D. Zhang, J. Li, H. Xie, Y. Ren, G. Qin, J. Magnesium Alloys 11 (2023) 4128–4145, doi:10.1016/j.jma.2023.11.002.
[14] J.M. Meier, J. Caris, A.A. Luo, J. Magnesium Alloys 10 (2022) 1401–1427, doi:10.1016/j.jma.2022.03.008.
[15] H.-y. Niu, K.-k. Deng, K.-b. Nie, C.-j. Wang, W. Liang, Y.-c. Wu, Mater. Chem. Phys. 249 (2020) 123131, doi:10.1016/j.matchemphys.2020.123131.
[16] D.H. Xiao, Z.W. Geng, L. Chen, Z. Wu, H.Y. Diao, M. Song, P.F. Zhou, Metallurgical&Materials Transactions A (2015), doi:10.1007/s11661-015-3053-7.
[17] J.H. Jiang, X. Geng, X.B. Zhang, Metals (Basel) (2023) 13, doi:10.3390/met13030446.
[18] S. Oh, M. Kim, K. Eom, J. Kyung, D. Kim, E. Cho, H. Kwon, Int. J. Hydrogen Energy 41 (2016) 5296–5303, doi:10.1016/j.ijhydene.2016.01.067.
[19] H.-y. Niu, K.-k. Deng, K.-b. Nie, F.-f. Cao, X.-c. Zhang, W.-g. Li, J. Alloys Compd. 787 (2019) 1290–1300, doi:10.1016/j.jallcom.2019.02.089.
[20] L. Chen, Z. Wu, D.H. Xiao, Z.W. Geng, P.F. Zhou, Mater. Corros. 66 (2015) 1159–1168, doi:10.1002/maco.201408090.
[21] Y. Zhang, X. Wang, Y. Kuang, B. Liu, K. Zhang, D. Fang, Mater. Lett. 195 (2017) 194–197, doi:10.1016/j.matlet.2017.02.024.
[22] L. Chen, G.-s. Huang, C. Zhang, D.-b. Xia, Y.-c. Zhao, F.-s. Pan, Mater. Sci. Technol. 33 (2017) 1312–1318, doi:10.1080/02670836.2017.1288691.
[23] C. Zhang, L. Wu, G. Huang, L. Chen, D. Xia, B. Jiang, A. Atrens, F. Pan, J. Mater. Sci. Technol. 35 (2019) 2086–2098, doi:10.1016/j.jmst.2019.04.012.
[24] J. Wang, S. Gao, X. Liu, X. Peng, K. Wang, S. Liu, W. Jiang, S. Guo, F. Pan, J. Magnesium Alloys 8 (2020) 127–133, doi:10.1016/j.jma.2019.11.010.
[25] K. Ma, J. Wang, Y. Peng, C. Dai, Y. Pan, D. Wang, Y. Wang, S. Pei, Y. Ma, J. Phys. Chem. Solids 171 (2022) 110974, doi:10.1016/j.jpcs.2022.110974.
[26] D. Wang, K. Dong, Z. Jin, K. Guan, F. Cao, H. Zhao, M. Zha, H.-Y. Wang, J. Alloys Compd. 914 (2022) 165325, doi:10.1016/j.jallcom.2022.165325.
[27] Z. Shi, M. Liu, A. Atrens, Corros. Sci. 52 (2010) 579–588, doi:10.1016/j.corsci.2009.10.016.
[28] A. Atrens, G.L. Song, M. Liu, Z. Shi, F. Cao, M.S. Dargusch, Adv. Eng. Mater. 17 (2015) 400–453, doi:10.1002/adem.201400434.
[29] M.C. Zhao, M. Liu, G. Song, A. Atrens, Corros. Sci. 50 (2008) 1939–1953, doi:10.1016/j.corsci.2008.04.010.
[30] F. Cao, Z. Shi, G.L. Song, M. Liu, A. Atrens, Corrosion Sci.: J. Environ. Degrad. Mater. Control (2013), doi:10.1016/j.corsci.2013.06.030.
[31] S. Yin, W. Duan, W. Liu, L. Wu, J. Yu, Z. Zhao, M. Liu, P. Wang, J. Cui, Z. Zhang, Corros. Sci. 166 (2020) 108419, doi:10.1016/j.corsci.2019.108419.
[32] K. Xu, S. Liu, Y. Du, L. Dreval, G. Cai, Z. Jin, J. Alloys Compd. 784 (2019) 769–787, doi:10.1016/j.jallcom.2018.12.377.
[33] X.D. Wang, W.B. Du, Z.H. Wang, K. Liu, S.B. Li, J. Rare Earths 30 (2012) 503–506, doi:10.1016/S1002-0721(12)60080-5.
[34] Z.H. Chen, T. Zhou, D. Chen, H.G. Yan, J.H. Chen, Mater. Sci. Technol. 24 (2008) 848–855, doi:10.1179/174328408X322097.

[35] T. Zhou, D. Chen, Z.H. Chen, Trans. Nonferrous Metals Soc. China 18 (2008) S101–S106, doi:10.1016/S1003-6326(10)60183-5.
[36] W. Guo, C. Wang, W. Ding, X. Yan, Y.G. Chen, Mater. Res. Express (2019).
[37] E. Maleki, F. Shahri, M. Emamy, Met. Mater. Int. (2019), doi:10.1007/s12540-019-00530-w.
[38] S. Feliu, Metals - Open Access Metallur. J. 10 (2020) 775, doi:10.3390/met10060775.
[39] W.-l. Cheng, S.-c. Ma, Y. Bai, Z.-q. Cui, H.-x. Wang, J. Alloys Compd. 731 (2018) 945–954, doi:10.1016/j.jallcom.2017.10.073.
[40] K.Y. Luo, C.Y. Wang, C.Y. Cui, J.Z. Lu, Y.F. Lu, J. Alloys Compd. 782 (2019) 1058–1075, doi:10.1016/j.jallcom.2018.12.224.
[41] J. Li, Q. Jiang, H. Sun, Y. Li, Corros. Sci. 111 (2016) 288–301, doi:10.1016/j.corsci.2016.05.019.
[42] W. Jin, G. Wu, H. Feng, W. Wang, X. Zhang, P.K. Chu, Corros. Sci. 94 (2015) 142–155, doi:10.1016/j.corsci.2015.01.049.
[43] D.H. Cho, B.W. Lee, J.Y. Park, K.M. Cho, I.M. Park, J. Alloys Compd. 695 (2017) 1166–1174, doi:10.1016/j.jallcom.2016.10.244.
[44] P.-Y. Wang, J.-G. Wang, C. Wang, J.-S. Li, Z.-M. Hua, H. Ju, M.-X. Li, M. Zha, H.-Y. Wang, Materialia (Oxf) 16 (2021) 101073, doi:10.1016/j.mtla.2021.101073.
[45] J. Rong, P.Y. Wang, M. Zha, C. Wang, X.Y. Xu, H.Y. Wang, Q.C. Jiang, J. Alloys Compd. 738 (2018) 246–254, doi:10.1016/j.jallcom.2017.11.348.
[46] J. Wang, T. Li, H.X. Li, Y.Z. Ma, J.S. Zhang, J. Magnesium Alloys (2020) 9, doi:10.1016/j.jma.2020.08.019.
[47] W. Tan, T. Li, S. Li, D. Fang, X. Ding, J. Sun, J. Mater. Sci. Technol. 94 (2021) 22–31, doi:10.1016/j.jmst.2021.04.010.
[48] Y.H. Liu, Z.R. Zhang, J. Wang, Y. Li, H.X. Li, L.Y. Jia, J.H. Wang, J.S. Zhang, J. Magnesium Alloys 11 (2023) 720–734, doi:10.1016/j.jma.2022.05.012.
[49] A. Dobkowska, B. Adamczyk – Cieślak, M. Koralnik, W. Chromiński, J. Kubasek, J. Ciftci, D. Kuc, J. Mizera, J. Magnesium Alloys 10 (2022) 811–820, doi:10.1016/j.jma.2021.08.020.
[50] J. Li, Y. Qiu, J. Yang, Y. Sheng, Y. Yi, X. Zeng, L. Chen, F. Yin, J. Su, T. Zhang, X. Tong, B. Guo, J. Magnesium Alloys 11 (2023) 217–229, doi:10.1016/j.jma.2021.04.007.
[51] T. Zheng, Y. Hu, S. Yang, J. Magnesium Alloys 5 (2017) 404–411, doi:10.1016/j.jma.2017.09.003.
[52] G.R. Argade, S.K. Panigrahi, R.S. Mishra, Corros. Sci. 58 (2012) 145–151, doi:10.1016/j.corsci.2012.01.021.
[53] S. Gollapudi, Corros. Sci. 62 (2012) 90–94, doi:10.1016/j.corsci.2012.04.040.
[54] K.D. Ralston, N. Birbilis, C.H.J. Davies, Scr. Mater. 63 (2010) 1201–1204, doi:10.1016/j.scriptamat.2010.08.035.
[55] Z.-Z. Jin, M. Zha, H.-Y. Wang, J.-G. Ma, Y.-C. Liu, Mater. Des. 234 (2023) 112345, doi:10.1016/j.matdes.2023.112345.
[56] Z.-Z. Jin, M. Zha, Z.-Y. Yu, P.-K. Ma, Y.-K. Li, J.-M. Liu, H.-L. Jia, H.-Y. Wang, J. Alloys Compd. 833 (2020) 155004, doi:10.1016/j.jallcom.2020.155004.
[57] Z.-Z. Jin, M. Zha, S.-Q. Wang, S.-C. Wang, C. Wang, H.-L. Jia, H.-Y. Wang, J. Magnesium Alloys 10 (2022) 1191–1206, doi:10.1016/j.jma.2022.04.002.
[58] S.M. He, X.Q. Zeng, L.M. Peng, X. Gao, J.F. Nie, W.J. Ding, J. Alloys Compd. 427 (2007) 316–323, doi:10.1016/j.jallcom.2006.03.015.